



#### Available online at www.sciencedirect.com

#### **ScienceDirect**

Geochimica et Cosmochimica Acta 280 (2020) 281-301

#### Geochimica et Cosmochimica Acta

www.elsevier.com/locate/gca

# The speciation of carbon, nitrogen, and water in magma oceans and its effect on volatile partitioning between major reservoirs of the Solar System rocky bodies

Damanveer S. Grewal a,\*, Rajdeep Dasgupta Alexandra Farnell a,b

a Department of Earth, Environmental, and Planetary Sciences, Rice University, 6100 Main Street, MS 126, Houston, TX 77005, USA
b St. John's School, 2401 Claremont Ln, Houston, TX 77019, USA

Received 20 November 2019; accepted in revised form 18 April 2020; Available online 28 April 2020

#### Abstract

The composition of atmospheres and the resulting potential for planetary habitability in the rocky bodies of our Solar System and beyond is strongly controlled by the volatile exchange between their silicate reservoirs and exospheres. The initial budget and speciation of major volatiles, like carbon (C), nitrogen (N) and water (H<sub>2</sub>O), in the silicate reservoirs and atmospheres was set during the formation stages of rocky bodies. However, the speciation of these major volatiles in reduced silicate melts prevalent during the differentiation stages of rocky bodies and its effect on the partitioning of volatiles between major rocky body reservoirs is poorly known. Here we present SIMS and vibrational spectroscopy (FTIR and Raman) data, determining C solubility, H content, and speciation of mixed C-O-N-H volatiles in graphite saturated silicate glasses from high P (1-7 GPa)-T (1500-2200 °C) experiments reported in Grewal et al. (2019b, 2019a). The experiments recorded oxygen fugacity (log fO2) between IW-4.3 and IW-0.8. C-O-N-H speciation varied systematically as function of  $fO_2$  at any given P-T. We find out that C-N<sup>-</sup>,  $CO_3^{2-}$ ,  $N_2$ , and OH<sup>-</sup> are the dominant species in the oxidized range (>IW-1.5), along with some contributions from C-H, N-H, and C-O bearing species. Between IW-3.0 and IW-1.5, C is bonded as C-O either in the form of isolated C-O molecules or Fe-carbonyl complexes, or as C-H in hydrocarbons, or as combination of both in esters, while almost all of the H is bonded with the dominant N species, i.e.,  $NH^{2-}$ or NH<sub>2</sub>. At the most reduced conditions (<IW-3.0), C is present mostly in the form of C-H bearing species, while anhydrous N<sup>3</sup> followed by N-H bearing molecules are the dominant N bearing species. Magma oceans (MOs) in highly reduced bodies like Mercury would contain most of their C as graphite if MO is carbon saturated and the dissolved C and N would be chemically bonded with the silicate network either in the form of anhydrous C<sup>4-</sup> and N<sup>3-</sup>, or hydrogenated C-H and N-H bearing species depending on H content of the silicate melts. MOs relevant for Mars, the Moon, Vesta, and angrite parent body would contain C and N mostly in the form of C-O and N-H bearing species, respectively. If the composition of Earth's accreting material evolved from reduced to oxidized, then initially a significant amount of the C and N budget would be locked in the silicate reservoirs, which would subsequently be released to the proto-atmosphere(s) at later stages. The retention of proto-atmosphere(s) formed by MO degassing on Earth could have provided important precursors for prebiotic chemistry which possibly led to the eventual habitability of our planet. Additionally, based on the dominant speciation of N versus C in silicate melt as a function of fO2, we also predict that  $D_{\rm N}^{\rm alloy/silicate}$  is unaffected by fH<sub>2</sub> under highly reduced conditions (<IW-3), while  $D_{\rm C}^{\rm alloy/silicate}$  is affected. Therefore, caution must be taken during the application of experimentally determined  $D_{\rm N}^{\rm alloy/silicate}$  and  $D_{\rm C}^{\rm alloy/silicate}$  to nominally anhydrous MOs. © 2020 Elsevier Ltd. All rights reserved.

Keywords: Carbon; Nitrogen; Water; Volatile speciation; Silicate melts; Magma oceans; Early atmospheres; Planetary habitability

<sup>\*</sup> Corresponding author.

E-mail address: dsg10@rice.edu (D.S. Grewal).

#### 1. INTRODUCTION

The release of volatiles via magmatic degassing has a primary control on the composition of atmospheres of rocky planets (e.g., Gaillard and Scaillet, 2014). The composition of gases released by magmatic degassing is directly controlled by the oxygen fugacity (fO2) of the silicate melts (Hirschmann, 2012; Ardia et al., 2013; Wetzel et al., 2013; Gaillard and Scaillet, 2014; Armstrong et al., 2015; Dalou et al., 2019b; Dasgupta and Grewal, 2019). Much attention has been paid in recent years to the atmospheric composition set by magmatic degassing during the last ~4 Ga on Earth and other rocky bodies like Mars, Mercury and the Moon (Wetzel et al., 2015; Li et al., 2017). Degassing of magma oceans (MOs) during their formation stages is thought to be responsible for setting the initial composition of planetary protoatmospheres (Hirschmann, 2012). However, the speciation of mixed volatiles in the natural silicate melts under the highly reduced conditions prevalent during the formation of rocky bodies is poorly known.

Core-mantle equilibration during MO events denotes interaction between the Fe-rich alloy and molten silicate reservoirs resulting in highly reduced conditions below the iron-wüstite buffer (IW) buffer (e.g., Rubie et al., 2011; Wade and Wood, 2005). The composition of silicate melts, in addition to the composition of the core forming alloy as well as temperature and pressure, control the core-mantle differentiation character of a volatile element (siderophile or lithophile). This affects the resulting abundances of these volatiles in post-core formation bulk silicate reservoirs (Hirschmann, 2012; Chi et al., 2014; Li et al., 2015; Li et al., 2016a; Dalou et al., 2017; Speelmanns et al., 2019; Grewal et al., 2019b; Grewal et al., 2019a). For example, while nitrogen (N) shows increasing lithophile character at  $<\sim$ IW – 2, it acts as a siderophile element at  $>\sim$ IW – 2 (Li et al., 2016b; Dalou et al., 2017; Speelmanns et al., 2019; Grewal et al., 2019a,b). The siderophile character of carbon (C) varies over an order of magnitude depending on the  $fO_2$ of alloy-silicate equilibration (Li et al., 2015; Li et al., 2016a). Variance in the intrinsic fO<sub>2</sub> of the accreting material and the modes of core-mantle differentiation mean that the volatile budgets of the silicate melts and the resulting compositions of proto-atmospheres could show large variations (Hirschmann, 2012; Dalou et al., 2017; Grewal et al., 2019a). For example, it is postulated that smaller planets like Mars and Mercury have undergone single-stage coremantle differentiation events but with widely different  $fO_2s$  (IW – 1 and IW – 5.5, respectively; Rai and Van Westrenen, 2013; Zolotov et al., 2013), whereas a larger rocky planet like Earth had a protracted growth history with several stages of alloy-silicate equilibration and gradation in the  $fO_2$  of the accreting material (IW – 5 to IW – 1; Wade and Wood, 2005; Rubie et al., 2011). Therefore, a large difference in the differentiation conditions of Earth, Mercury, and Mars had the potential to strongly affect their volatile budgets as well as the resulting volatile cycling in these planets.

Previous studies show that fO2 controls C-O-N-H speciation in the silicate melts during and/or immediately post core-mantle differentiation. Molecular CO<sub>2</sub>,CO<sub>3</sub><sup>2-</sup>, N<sub>2</sub>, H<sub>2</sub>O, and OH<sup>-</sup> are the dominant dissolved species in the silicate melts under relatively oxidized conditions (>IW-1), while under increasingly reduced conditions  $(\le IW - 1)$  dissolution in reduced forms like C-H, C-O, N-H, N<sup>3-</sup> and H<sub>2</sub> becomes dominant (Mysen et al., 2008; Mysen and Fogel, 2010; Mysen et al., 2011; Kadik et al., 2013; Armstrong et al., 2015; Kadik et al., 2015; Kadik et al., 2017; Dalou et al., 2019b; Mosenfelder et al., 2019; Grewal et al., 2019b). None of the above studies have combined quantitative and spectroscopic analyses to detail the effect of variation in  $fO_2$ , with varying P, T, and silicate melt composition (NBO/T; a measure of degree of silicate melt polymerization, is expressed as total non-bridging oxygens per tetrahedral cations; NBO/T =  $(2 \times \text{Total O})/T - 4$ , where T = Si + Ti + Al + Cr + P (e.g., Mysen et al., 1982)), on the dissolution of mixed C-O-N-H volatiles in the silicate melts prevalent during a wide range of MO conditions. Mysen et al. (2008), Mysen and Fogel (2010), Mysen et al. (2011), Kadik et al. (2013), Kadik et al. (2015), and Kadik et al. (2017) presented FTIR and Raman spectroscopy data for mixed C-O-N-H volatiles in relatively simple silicate melt compositions and/or in a limited fO<sub>2</sub> range  $(\log fO_2 > IW - 2.7)$  without any quantification of C and H contents in the silicate melts. Dalou et al. (2019b) and Grewal et al. (2019b) provided only Raman spectroscopy data in a relatively oxidized range ( $log fO_2 > -$ IW - 2.1). Although Armstrong et al. (2015) provided FTIR and Raman data for C-O-N-H speciation data over a wide  $fO_2$  range (between IW – 3.6 and IW + 1.5), N was an incidental contaminant in almost all of their experiments which did not allow for the possibility to study the transformation of N speciation with fO<sub>2</sub>. Mosenfelder et al. (2019) provided FTIR spectra for C-O-N-H speciation data but the Fe-free nature of their silicate glasses did not allow for fO<sub>2</sub> estimation and subsequent analysis of evolution of C-O-N-H speciation with change in fO<sub>2</sub>. Additionally, none of the previous studies provide a systematic comparison of the abundance and spectroscopic characterization of C-O-N-H volatiles to predict whether C and N contents and species predicted by the substantially hydrated experiments also hold true for anhydrous MOs. Water content of enstatite chondrites (meteorites representative of the inner Solar System reservoir) is not fully known. Whereas some earlier studies reported between 0.6 (EH4) to 4.6 wt. % (EL6) of equivalent H<sub>2</sub>O in enstatite chondrites (Yang and Epstein, 1983; Jarosewich, 1990; Robert, 2003), recent studies argue that enstatite chondrites accreted little to no water (Brearley, 2006; Ruzicka and Hutson, 2006; Alexander, 2017). If the earliest forming protoplanets in the inner Solar System potentially accreted in nominally anhydrous conditions (Morbidelli et al., 2012; Alexander, 2017; Alexander et al., 2018), it is essential to constrain whether experimentally determined  $D_N^{\text{alloy/silicate}}$ and D<sub>C</sub> alloy/silicate values are directly applicable for anhydrous to water-poor MOs. Therefore, a systematic dataset is required, which combines C-O-N-H abundance and speciation to constrain the dissolution mechanism of major volatiles in anhydrous and hydrous MOs and their effect on the distribution of volatiles in the rocky body reservoirs.

In this study we present FTIR and Raman spectroscopy data for the experimental glasses generated in Grewal et al. (2019b, 2019a). We also report C solubility and H contents of silicate glasses obtained using SIMS analysis for experiments presented in Grewal et al. (2019b). By combining the FTIR and Raman spectrographic analyses with bulk N, C, and H concentrations of the silicate glasses, we demonstrate the effect of  $fO_2$ , with variation of P, T and NBO/T, on the speciation of C-O-N-H volatiles in reduced silicate melts. We use the experimental results to predict the speciation of C-O-N-H volatiles in a variety of MO settings applicable for an assortment of rocky bodies in our Solar System. Through constraining the speciation of C-O-N-H volatiles in silicate magma ocean-relevant conditions, we comment on the relative distribution of carbon and nitrogen between the core, MO and the overlying proto-atmosphere.

#### 2. METHODS

#### 2.1. Experimental details

The silicate glasses used in this study were synthesized in Grewal et al. (2019b, 2019a) at 1-7 GPa, 1500-2200 °C,  $\log fO_2 \sim IW-4.3$  to IW-0.8 and NBO/T = 0.4-2.2. All experiments were performed in graphite capsules using alloy-silicate mixtures containing ~30-35 wt.% alloy and 65–70% wt.% silicate. Experiments were conducted either by loading a single starting composition into a graphite capsule or by loading 3-4 starting compositions in a single graphite stock by drilling separate sample chambers. Fine powders of Fe<sub>4</sub>N, Fe<sub>7</sub>N<sub>3</sub> or Si<sub>3</sub>N<sub>4</sub> were the source of N and the N content was fixed at ~1.5-1.7 wt.%. in all of the starting mixtures. Eight different silicate mixtures reported in Grewal et al. (2019b, 2019a) were used to constraint the effect of silicate melt composition. The experiments were performed using either an end-loaded piston cylinder (PC) apparatus, or an 1100-ton Walker-type multi-anvil (MA) device at Rice University. An experimental duration of 5-300 minutes was deemed sufficient to attain chemical equilibrium. Water was not added in any of the experimental powders and is present primarily due to the adsorption of moisture in the starting materials. This led to limited variation in fH2O during the experimental conditions.

Post de-pressurization, single-chambered samples were cut longitudinally into two halves while multi- chambered samples were cut transversely into two halves using a tungsten wire saw. Both halves of the samples were mounted in Crystalbond<sup>TM</sup>, ground using 1200-grit sandpaper and polished using 0.3-micron alumina slurry on a velvet cloth. The polished halves were soaked in acetone overnight to remove Crystalbond<sup>TM</sup>. The following analytical techniques were used in the order: (1) Electron microprobe: To determine N as well as major and minor elemental composition

(details in Grewal et al. (2019b, 2019a)) in alloy and silicate phase. (2) Secondary Ion Mass Spectrometry: To determine bulk C and H contents in silicate phase. (3) Raman spectroscopy: To determine C-O-N-H speciation in silicate phase. 4) Fourier transform infrared spectroscopy: To determine C-O-N-H speciation in silicate phase. One half of each sample was used for the analytical techniques: (1), (2), and (3), while the other half was used for technique: (4).

#### 2.2. Analytical details

N along with major and minor elemental abundances of the experimental phases were measured using a JEOL JXA8530F Hyperprobe and reported in Grewal et al. (2019b, 2019a).

#### 2.2.1. Secondary Ion Mass Spectrometry (SIMS)

Bulk C and H contents of the silicate melts from Grewal et al. (2019a) that quenched to glasses or had glassy pools were determined by using Cameca IMS 1280 ion microprobe at Woods Hole Oceanographic Institution following the procedural details listed in previous studies Chi et al. (2014) and Dasgupta et al. (2013). Re-polished samples were placed in indium substrate in an aluminum dish and gold-coated followed by placing them under vacuum for at least 24 h before analysis. A beam of <sup>133</sup>Cs<sup>+</sup> ions with 1-1.5nA current and 12 kV energy was used to focus on a spot size of 10 µm in diameter followed by rastering over a  $30 \times 30 \,\mu m$  area. Negatively charged ions were accelerated at 10 kV into a double-focusing mass spectrometer. The central  $15 \times 15$  µm of the beam-rastered area was analyzed by placing a mechanical aperture in the focal plane of secondary ion optics, thereby minimizing any potential surface carbon contamination in the measurement. 4-6 spots per sample were pre-sputtered for 240 s and then measured over at least 10 cycles of ion intensities. During each cycle <sup>12</sup>C, <sup>1</sup>H<sup>16</sup>O and <sup>30</sup>Si were recorded and intensity ratios of <sup>12</sup>C/<sup>30</sup>Si and <sup>1</sup>H<sup>16</sup>O/<sup>30</sup>Si were converted to C and H<sub>2</sub>O concentrations using the calibration curves developed in the same analytical session (Dasgupta et al., 2013; Chi et al., 2014; Li et al., 2015; Grewal et al., 2019b). After every 8-10 spots on the sample glasses, 2–3 analyses were performed on the standard glass (ALV519-4-1) to check for possible deviations during the measurements.

#### 2.2.2. Raman spectroscopy

C-O-N-H speciation in the silicate glasses from Grewal et al. (2019a) was determined with a Renishaw inVia Raman microscope at the shared equipment authority of Rice University (Fig. 1). A 514 nm laser was used to obtain the spectral data in the frequency range of  $200-5000 \text{ cm}^{-1}$  at a resolution of 1 cm<sup>-1</sup> with a  $50\times$  objective lens at an output power of 23 mW. To increase the signal/noise ratio, spectra at each point were accumulated five times with an exposure time set at 30 s. The contribution of atmospheric  $N_2$  was accounted for by recording a Raman spectrum of the air and then subtracting this blank signal from the acquired Raman spectrum of the sample (Roskosz et al., 2006). The final reported Raman spectra for each sample

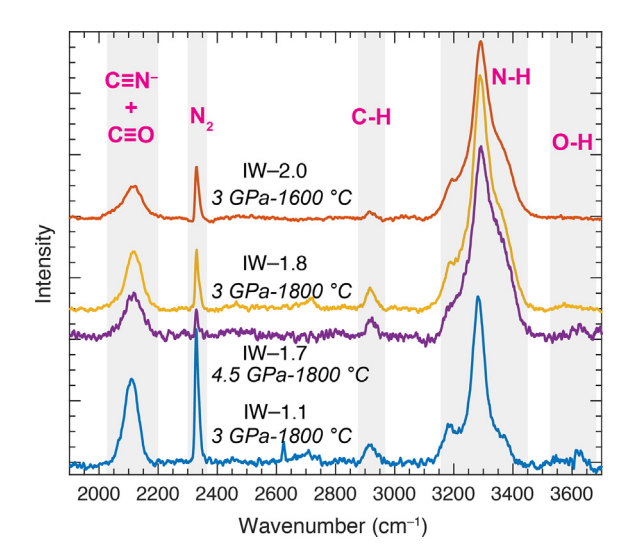


Fig. 1. Typical background corrected Raman spectra of the peaks associated with C-O-N-H species in the experimental silicate glasses under graphite saturated conditions. Isolated  $C \equiv O$  molecules or complexes,  $C \equiv N^-$  complexes, isolated  $N_2$  molecules, and chemical interactions of C-H, N-H, and O-H bearing species with the silicate melt structure define the volatile dissolution pattern in the glasses.

were averaged and smoothed followed by the relevant background correction and peak deconvolution using the OriginPro software package (OriginLab®).

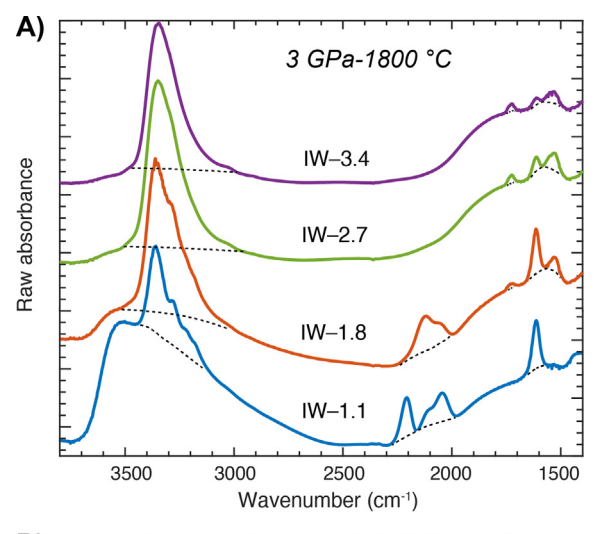
#### 2.2.3. Fourier transform infrared spectroscopy (FTIR)

FTIR spectra were obtained by using a Thermo Nicolet Fourier Transform Infrared Spectrometer at the Department of Earth, Environmental and Planetary Sciences of Rice University (Fig. 2). All experimental glasses were doubly polished to thickness of 50-250 µm and cleaned with acetone and ethanol before a given analytical session. A digital micrometer (ID-C125EXB Mitutoyo Digimatic Indicator) was used to measure the sample thickness. Liquid nitrogen was used overnight before every analytical session to remove atmospheric gas contamination. Blank backgrounds were collected at the beginning of each spectral analysis. FTIR spectra were collected on at least three to four spots per sample (Fig. S1). Each spectrum was obtained in the frequency range of 650–4000 cm<sup>-1</sup> with a resolution of 4 cm<sup>-1</sup> and 128 scans using a  $100 \times 100 \,\mu m$ spot. The final reported spectra represent the averaged values for each sample. Background correction and peak deconvolution for the final reported FTIR spectra for each sample was done using the OriginPro software package.

A peak attributed to O-H stretching at  $\sim 3530 \text{ cm}^{-1}$  was used to determine the amount of bulk H bonded with O. The peak area and height of O-H stretching in each spectrum was determined using a cubic spline background. The concentration of bulk H dissolved as OH/H<sub>2</sub>O was quantified by using the Beer-Lambert Law:

$$C_{\rm x} = 100 * M_{\rm x} A_{\rm y} / d\rho \varepsilon_{\rm y}$$

where,  $C_x$  is the concentration of the volatile species x in the sample,  $M_x$  is the molecular weight of the volatile species  $\times$  (18.02 gmol<sup>-1</sup> for H<sub>2</sub>O),  $A_y$  is the absorption of peak y



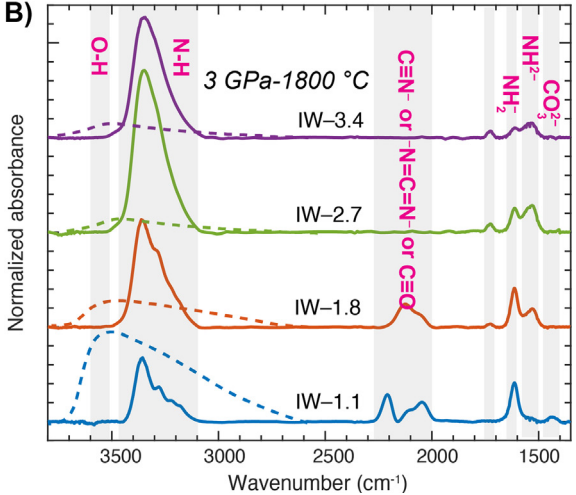


Fig. 2. Typical (A) raw and (B) background corrected, thickness normalized FTIR spectra of the peaks associated with C-O-N-H species in the experimental silicate glasses under graphite saturated conditions over a wide  $fO_2$  range and at a fixed P-T. The dashed curves in (A) represent the spline background corrections. The dashed curves in (B) show the broad asymmetric peak of O-H vibration post-deconvolution from N-H stretching frequency in the similar range. Chemical interactions of  $C \equiv N^-$ ,  $N = C = N^-$ ,  $CO_3^{2-}$ ,  $C \equiv O$ , esters, N-H, and O-H bonds with the silicate melt structure define C-O-N-H interaction with the silicate melt structure.

(peak height measured from the spectrum in cm<sup>-1</sup>), d is the density of the sample (in gL<sup>-1</sup>), and  $\varepsilon_y$  is the extinction coefficient for the peak (in Lmol<sup>-1</sup>cm<sup>-1</sup> for linear extinction coefficient). We used a fixed  $\varepsilon$  value of 67 Lmol<sup>-1</sup>cm<sup>-1</sup> for OH<sup>-</sup> at ~3550 cm<sup>-1</sup> (Stolper, 1982). Although extinction coefficient is expected to vary with silicate melt composition (King et al., 2002; Mandeville et al., 2002), only few discrete extinction coefficient values are available for a given volatile species for different compositions. Therefore, our use of a fixed value for  $\varepsilon$  is justified as the relative change of speciation at different  $fO_2$ s is the primary goal of this study. Average composition determined by electron microprobe (reported in Grewal et al. (2019b, 2019a)) was

used to determine the density of the silicate glasses using the method of Silver (1988).

#### 2.3. Peak fitting procedure

Baseline correction, peak deconvolution and curve fitting of the Raman and FTIR spectra were performed using the OriginPro software package. A spline baseline at small intervals, accounting for different curvatures at different wavenumbers, was set in the  $\sim 1400-2500 \text{ cm}^{-1}$  portion of the FTIR spectra. Special care had to be taken to apply the baseline correction in ~2500–3800 cm<sup>-1</sup> range because of the O-H stretching frequency which has a broad asymmetric peak at  $\sim 3550-3580 \text{ cm}^{-1}$  (Fig. 2A). The curvature for this peak extends over a wide range (~2800–3800 cm<sup>-1</sup>) thereby interfering with N-H stretching frequency lying in a similar range ( $\sim 3150-3380 \text{ cm}^{-1}$ ). Therefore, to decouple the contribution of O-H and N-H speciation in the spectral signals, asymmetric curved backgrounds were set in the  $\sim$ 2500–3800 cm<sup>-1</sup> range that account for the contribution of the asymmetric O-H peak (Fig. 2A).

After applying the baseline correction, FTIR spectra was deconvoluted to Lorentzian components in order to quantify the proportions of the C-O-N-H species dissolved in the silicate melt. The locations of the peaks, the bandwidth (accounted by FWHM: Full Width at Half Maximum), band intensity, and area under the fitted curve were treated as independent parameters. The convergence criterion for each spectrum was determined by minimum chi-squared estimation ( $\chi^2$ ) scheme.

#### 3. RESULTS

#### 3.1. Texture of experimental products

All of the experiments reported in Grewal et al. (2019b, 2019a) had quenched metal blobs embedded in silicate melt. Only the experiments that had uniform glassy textures were used for measurements in this study (Fig. S2). All of the analyzed silicate glasses had uniform glassy structure with no evidence of bubbles (Fig. S2). Therefore, all of the data reported in this study are for fluid-undersaturated experiments. Additional textural details for the experimental products can be found in Grewal et al. (2019b, 2019a).

#### 3.2. Estimation of oxygen fugacity

Oxygen fugacity ( $fO_2$ ) of the experimental products was determined via the co-existence of Fe-rich alloy melt and silicate melt:

$$FeO^{silicate\ melt} = Fe^{alloy\ melt} + 1/2\ O_2$$
 (1)

from which  $fO_2$  relative to  $fO_2$  of the iron-wüstite buffer (IW), at a given P-T, is defined by:

$$\mathrm{IW} = 2\mathrm{log} \frac{a_{\mathrm{FeO}}^{\mathrm{silicate \ melt}}}{a_{\mathrm{Fe}}^{\mathrm{alloy \ melt}}} = 2\mathrm{log} \frac{X_{\mathrm{FeO}}^{\mathrm{silicate \ melt}} \gamma_{\mathrm{FeO}}^{\mathrm{silicate \ melt}}}{X_{\mathrm{Re}}^{\mathrm{alloy \ melt}} \eta_{\mathrm{Fe}}^{\mathrm{alloy \ melt}}} \tag{2}$$

where,  $a_{\rm FeO}^{\rm silicate\ melt}$  is the activity of FeO component in silicate melt and  $a_{\rm Fe}^{\rm alloy\ melt}$  is the activity of Fe component in alloy melt;  $X_{\rm FeO}^{\rm silicate\ melt}$  and  $\gamma_{\rm FeO}^{\rm silicate\ melt}$  is the mole fraction and activity coefficient of FeO component in silicate melt, respectively;  $X_{\rm Fe}^{\rm alloy\ melt}$  and  $\gamma_{\rm Fe}^{\rm alloy\ melt}$  is the mole fraction and activity coefficient of Fe component in alloy melt, respectively. Using the non-ideal solution model,  $fO_2$  was calculated assuming a fixed  $\gamma_{\rm FeO}^{\rm silicate\ melt}$  of 1.5 (Holzheid et al., 1997). To account for the non-ideal interactions between components of the alloy melt,  $\gamma_{\rm Fe}^{\rm alloy\ melt}$  was calculated via approach in Wagner equations (Ma, 2001) using the 'Online Metal Activity Calculator' (http://norris.org.au/expet/metalact/).

### 3.3. Bulk carbon solubility and hydrogen content in the silicate melt

Bulk C and H content in the silicate melts determined using SIMS in this study and from Grewal et al. (2019b) are tabulated in Table 1 along with the bulk N content reported in Grewal et al. (2019b, 2019a). Bulk H content varies from 189 to 1293 ppm (except one experiment containing 2330 ppm H). The range of bulk H variation in this study is similar to the measurements of previous experimental studies conducted in a similar P-T-fO2 range (e.g., Dalou et al., 2017; Li et al., 2015, 2016), where no H<sub>2</sub>O was intentionally added in the starting mixtures. The variation of graphite saturated C content of the silicate melts in the range of 81-977 ppm is consistent with the values reported in several previous studies for N-free (Wetzel et al., 2013; Dasgupta et al., 2013; Stanley et al., 2014; Chi et al., 2014; Armstrong et al., 2015; Li et al., 2015; Li et al., 2016a; Duncan et al., 2017; Li et al., 2017; Tsuno et al., 2018) and N-bearing systems (Dalou et al., 2017; Grewal et al., 2019b). Broadly, the C content decreases with decreasing fO2 as observed in previous studies (Dasgupta and Grewal, 2019 and references therein).

#### 3.4. Raman spectra

Across the range of 1300-4500 cm<sup>-1</sup>, Raman spectra were used to identify the structural interaction between dissolved C-O-N-H species and the silicate melt structure for glasses at  $log fO_2 > IW - 2.5$ . Due to extreme fluorescence, Raman spectra at  $\log fO_2 \le IW - 2.5$  did not yield volatile speciation information. Typical background corrected Raman spectra from IW - 2.5 to IW - 0.8 are shown in Fig. 1. Raman spectra show a variety of peaks for mixed C-O-N-H dissolution which can be ascribed to the presence of N-N, N-H, C-H, C-N, C-O and O-H bonds in the silicate melt structure. The intensities of peaks at ~2110 cm<sup>-</sup>  $2330 \text{ cm}^{-1}$ , and  $2930 \text{ cm}^{-1}$  drop with a decrease in  $fO_2$ . At least four peaks within  $\sim$ 3180 and 3370 cm<sup>-1</sup> overlap to show the prominent spectral feature within that range whose cumulative peak area increases with a decrease in  $fO_2$ .

Table 1
Summary of experimental conditions, oxygen fugacity, abundances of carbon, nitrogen, and hydrogen and normalized area under the fitted FTIR curves for different peaks.

Exp No.	P (GPa)	<i>T</i> (° C)	<sup>a</sup> Starting composition	blog fO <sub>2</sub> (IW)	°NBO/ T	Raman	FTIR	<sup>d</sup> N (wt. %)	°C (ppm)	eH-SIMS (ppm)	fH-FTIR (ppm)	<sup>g</sup> 1530: NH <sup>2-</sup>	g1610: NH <sub>2</sub>	g1730: Ester	<sup>g</sup> 2130: CO	<sup>g</sup> 2210: CN	<sup>g</sup> 3200- 3380:N- H
MA178- 10S	4.5	1800	70%ThB1 + 30%Fe- 5Ni-5N-10S	-0.85	0.98	×	×	0.25	927 (18)	728(33)	n.a.	n.a.	n.a.	n.a.	n.a.	n.a.	n.a.
MA178-0S	4.5	1800	70%ThB1 + 30%Fe- 5Ni-5N	-0.94	0.93	×	~	0.32 (4)	977 (42)	841(21)	n.a.	2.40 (16)	4.98 (14)	0	0	12.16 (33)	20.57 (200)
G483	3	1600	67%BCR + 33%Fe- 5Ni-5N	-0.96	0.62	<b>/</b>	~	0.39 (6)	202	336(6)	57(16)	1.58 (18)	3.13 (10)	0	0	0	21.54
G496	3	1800	70%ThB1 + 30%Fe- 5Ni-5N-10S	-0.97	0.95	<b>/</b>	~	0.15	543 (50)	671(43)	116(32)	1.70 (13)	3.41 (11)	0	0	9.78 (19)	<i>32.03 (376)</i>
G493	3	1600	70%ThB1 + 30%Fe- 5Ni-5N-10S	-1.01	0.92			0.09	259 (24)	730(47)	212(19)	o	4.32 (7)	0	0	3.36 (7)	21.42 (128)
G545_1d	1	1600	70%MO#1 + 30%Fe- 5N	-1.02	1.06			0.06	272 (18)	748(17)	212(30)	0.45(4)	2.03(5)	0	0	0.97	5.55(20)
G549_4	1	1700	70%MO#2 + 30%Fe- 5N	-1.02	1.25			0.06	292	803(32)	168(13)	0	1.35(7)	0	0	0.96 (10)	2.13(25)
G503	2	1600	70%ThB1 + 30%Fe- 5Ni-5N-10S	-1.05	0.89	<b>/</b>	×	0.07	299 (27)	965(62)	n.a.	n.a.	n.a.	n.a.	n.a.	n.a.	n.a.
G498	3	1600	70%ThB1 + 30%Fe- 5Ni-5N	-1.06	0.97	<b>/</b>	~	0.09	311 (28)	1190(77)	289(27)	1.51 (15)	6.05 (13)	0	0	3.75 (13)	26.00 (106)
G516	2	1600	70%ThB1 + 30%Fe- 5Ni-5N	-1.07	0.89	<b>/</b>	×	0.07	271 (15)	756(65)	n.a.	n.a.	n.a.	n.a.	n.a.	n.a.	n.a.
G499	3	1800	70%ThB1 + 30%Fe- 5Ni-5N	-1.08	0.90			0.19	652 (59)	1082(70)	243(31)	0.34 (11)	12.93 (17)	0	0	9.92 (18)	<i>57.30 (283)</i>
G545_3c	1	1600	70%MO#2 + 30%Fe- 5N	-1.09	1.22			0.06	272 (15)	838(54)	270(28)	0.23(5)	2.50 (11)	0	0	1.14 (5)	5.83(12)
G549_3	1	1700	70%MO#3 + 30%Fe- 5N	-1.10	1.56			0.04	333 (59)	854(27)	153(13)	0	2.51 (24)	0	0	0.88 (5)	2.75(12)
G549_1	1	1700	70%MO#4 + 30%Fe- 5N	-1.10	1.84			0.04 (2)	302	842(61)	302(33)	1.40(5)	3.76(9)	0	0	1.37 (9)	2.47(78)
G545_4a	1	1600	70%MO#3 + 30%Fe- 5N	-1.13	1.56			0.03 (2)	282	891(9)	241	0	1.89(5)	0	0	0.57 (6)	3.88(11)
G549_2	1	1700	70%MO#1 + 30%Fe- 5N	-1.13	0.98		×	0.07	238 (4)	789(6)	n.a.	n.a.	n.a.	n.a.	n.a.	n.a.	n.a.
G545_2b	1	1600	70%MO#4 + 30%Fe- 5N	-1.15	1.81	<b>/</b>		0.03 (2)	282 (7)	908(46)	244(22)	n.a.	n.a.	n.a.	n.a.	n.a.	n.a.
G517	1	1600	70%ThB1 + 30%Fe- 5Ni-5N	-1.17	0.86	<b>/</b>	X	0.03	300 (16)	1022(88)	n.a.	n.a.	n.a.	n.a.	n.a.	n.a.	n.a.
G515	1	1600	70%ThB1 + 30%Fe- 5Ni-5N-20S	-1.18	0.90	<b>/</b>	X	0.02	197 (27)	867(74)	n.a.	n.a.	n.a.	n.a.	n.a.	n.a.	n.a.
G504	1	1600	70%ThB1 + 30%Fe- 5Ni-5N-10S	-1.19	0.95	~	X	0.03	253 (24)	965(62)	n.a.	n.a.	n.a.	n.a.	n.a.	n.a.	n.a.

G488	3	1600	67%BCR + 33%Fe- 5Ni-5N-20S	-1.21	0.71	~	~	0.34 (6)	376 (29)	1054(21)	221(26)	0	4.48 (10)	0	0	4.93 (12)	28.11 (170)
G495	3	1800		-1.29	0.97	~	X	0.07	561 (31)	504(81)	n.a.	n.a.	n.a.	n.a.	n.a.	n.a.	n.a.
MA178- 20S	4.5	1800	70%ThB1 + 30%Fe- 5Ni-5N-20S	-1.31	0.95	×	×	0.19 (4)	760 (45)	831(17)	n.a.	n.a.	n.a.	n.a.	n.a.	n.a.	n.a.
G491	3	1600	67%ThB + 33%Fe-5Ni- 5N-20S	-1.37	0.93	~	<b>/</b>	0.06	339 (31)	2330 (151)	386(27)	6.85 (35)	9.29 (22)	0	0	0	34.40 (199)
G484	3	1600	67%BCR + 33%Fe 5Ni + 5N + 20S	-1.43	0.68			0.29 (7)	310 (5)	1293(16)	385(13)	0	5.82 (10)	0	0	3.47 (14)	32.41 (142)
MA214- 0S_7.5Si	6	1800	5Ni + 5N-0S-7.5Si	-1.48	0.66			0.82 (14)	248 (5)	899(18)	31	7.67 (16)	1.63 (11)	0.47(8)	0	0	142.89 (1711)
MA147- N-07	4	1800	5N-7.5Si	-1.65	0.61	×	×	1.82	748 (31)	1013(33)	n.a.	n.a.	n.a.	n.a.	n.a.	n.a.	n.a.
G427-N- 03	2		70%ThB + 30%Fe-5Ni- 5N-7.5Si	-1.66	0.68	×	X	0.13 (8)	306 (8)	493(8)	n.a.	n.a.	n.a.	n.a.	n.a.	n.a.	n.a.
G514	2	1800	70%ThB1 + 30%Fe- 5Ni-5N-20S	-1.71	1.57	<b>/</b>	X	0.05	393 (26)	244(21)	n.a.	n.a.	n.a.	n.a. 0	n.a.	n.a. 0	n.a.
MA213- 0S_7.5Si G554-0S-	4.5		70%ThB1 + 30%Fe- 5Ni-5N-0S-7.5Si 70%ThB1 + 30%Fe-	-1.74 $-1.78$	0.58		<i>✓</i>	1.30 (7) 0.78	312 (10) 304	868(17)	61(8)	12.00 (35) 9.15	11.04 (26) 13.04	0	13.77 (74) 16.08	0	162.57 (1769) 125.22
7.5Si G522-10S	1	1600	5Ni-5N-0S-7.5Si	-1.78 -1.92	0.62	×	<b>✓</b>	0.78 (11) 0.12	(11) 169	820(23) 444(5)	69(11)	(39) 3.33	(31)	0	(102) 2.84	0	(520) 29.38
G522-108 G511	3	1600	5Ni-5N-10S-7.5Si 70%ThB1 + 30%Fe-	-1.92 $-2.01$	0.59	^ /	<b>✓</b>	(6) 0.48	(2) 136	599(36)	43(5) 66(11)	(0.35) 9.71	(14) 12.64	0	(10) 3.49	0	(169) 125.03
G520-0S	2	1600	5Ni-5N-0S-7.5Si 70%ThB1 + 30%Fe-	-2.01 -2.02	0.56	×	×	(5) 0.67	(11) 224	556(11)	n.a.	(22)	(16)				(816) n.a.
G509	3	1600	5Ni-5N-7.5Si 70%ThB1 + 30%Fe-	-2.02	0.59	×	^	(9) 0.43	(39) 113	554(8)	75(8)	n.a. 5.58	n.a. 8.79	n.a. 0	n.a. 4.97	n.a. 0	82.58
G520-10S	2	1600	5Ni-5N-10S-7.5Si	-2.02	0.57	×	×	(4) 0.58	(10) 172	467(11)	n.a.	(15) n.a.	(12) n.a.	n.a.	(20) n.a.	n.a.	(639) n.a.
MA214-	6		5Ni-5N-10S-7.5Si 70%ThB1 + 30%Fe-	-2.13	0.49	×	×	(5) 1.58	(14) 123	741(21)	n.a.	n.a.	n.a.	n.a.	n.a.	n.a.	n.a.
0S_12.5Si G457-N-	2	1800	5Ni-5N-12.5Si	-2.22	0.54	×	^ /	(33) 1.19	(1) 300	453(7)	30(6)	4.65	4.28	0	7.89	0	72.67
06 G510	3	1600	5N-7.5Si	-2.24	0.60	``  -	<u></u>	(27) 0.44	(22) 176	1034(28)	161(23)	(27) 2.57	(20) 20.60	0	(247) 4.96	0	(429) 138.95
MA213-	4.5	1800	5Ni-5N-20S-7.5Si 70%ThB1 + 30%Fe-	-2.28	0.52	×	· •	(4) 1.81	(6) 195	978(24)	59(10)	(18) 15.33	(18) 10.59	1.60	(35)	0	(601) 211.65
0S_12.5Si G520-20S	2	1600	5Ni-5N-12.5Si	-2.35	0.71	×	×	(21) 0.51	(5) 237	578(11)	n.a.	(42) n.a.	(30) n.a.	(22) n.a.	n.a.	n.a.	(1904) n.a.
G432-N-	2	1750	5Ni-5N-20S-7.5Si 70%ThB + 30%Fe-5Ni-	-2.36	0.47	×	<b>/</b>	(6) 0.57	(24) 219	185(5)	28(5)	0	2.55	0	12.54	0	48.60
04 G437-N-	2	1800	5N-7.5Si 70%ThB + 30%Fe-5Ni-	-2.38	0.49	×	<b>/</b>	(16) 1.15	(28) 308	556(3)	36(7)	3.58	2.23	0	(106) 5.26	0	(429) 63.67
05			5N-7.5Si					(22)	(16)	. ,	` '	(23)	(17)		(16)		(619)

Exp No.	P (GPa)	<i>T</i> (° C)	<sup>a</sup> Starting composition	blog fO <sub>2</sub> (IW)	°NBO/ T	Raman	FTIR	<sup>d</sup> N (wt. %)	°C (ppm)	eH-SIMS (ppm)	fH-FTIR (ppm)	<sup>g</sup> 1530: NH <sup>2-</sup>	g1610: NH <sub>2</sub>	g1730: Ester	<sup>g</sup> 2130: CO	<sup>g</sup> 2210: CN	<sup>g</sup> 3200- 3380:N- H
G522-0S	1	1600	70%ThB1 + 30%Fe- 5Ni-5N-7.5Si	-2.43	0.56	×	~	0.26 (8)	229 (91)	244(4)	49(4)	3.14 (23)	3.73 (16)	0	1.74 (12)	0	30.87 (131)
G420-N- 01	2	1500	70%ThB + 30%Fe-5Ni- 5N-7.5Si	-2.64	0.51	×	<b>/</b>	1.01 (25)	108 (12)	333(7)	22(2)	6.63	2.97 (24)	0	4.93 (24)	0	70.53 (482)
G425-N- 02	2	1600	70%ThB + 30%Fe-5Ni- 5N-7.5Si	-2.71	0.51	×	×	1.10 (29)	152 (21)	354(9)	n.a.	n.a.	n.a.	n.a.	n.a.	n.a.	n.a.
G522-20S	1	1600	70%ThB1 + 30%Fe- 5Ni-5N-20S-7.5Si	-2.71	0.56	×		0.30 (5)	267 (45)	189(4)	44(5)	2.69 (43)	2.93 (25)	0	0.59 (5)	0	23.03 (133)
G554-0S- 12.5Si	3	1800	70%ThB1 + 30%Fe- 5Ni-5N-12.5Si	-2.74	0.48	×	~	2.32 (14)	139	775(10)	41(7)	14.35	6.99 (27)	1.87 (19)	0	0	238.07 (2284)
G525-10S- 12.5Si	3	1600	70%ThB1 + 30%Fe- 5Ni-5N-10S-12.5Si	-2.99	0.48	×	~	1.22	158	678(7)	35(3)	14.10 (34)	5.60 (22)	2.32 (15)	4.88 (33)	0	198.66 (1930)
MA214- 0S 17.5Si	6	1800	70%ThB1 + 30%Fe- 5Ni-5N-17.5Si	-3.11	0.41	×	×	2.97 (23)	136	738(11)	n.a.	n.a.	n.a.	n.a.	n.a.	n.a.	n.a.
G526-10S- 12.5Si	2	1600	70%ThB1 + 30%Fe- 5Ni-5N-10S-12.5Si	-3.11	0.49	×	~	0.95	149 (10)	722(11)	25(3)	9.83 (68)	2.87 (54)	0	0	0	180.21 (1531)
G526-0S- 12.5Si	2	1600	70%ThB1 + 30%Fe- 5Ni-5N-12.5Si	-3.20	0.47	×	<b>/</b>	1.25 (17)	122	622(11)	14(2)	1.10 (34)	0	0	0	0	107.43 (949)
G526-0S- 17.5Si	2	1600	70%ThB1 + 30%Fe- 5Ni-5N-17.5Si	-3.20	0.47	×	~	1.29	81(3)	456(11)	49(7)	16.92 (65)	11.75 (48)	0	0	0	234.30 (1805)
MA213- 0S 17.5Si	4.5	1800	70%ThB1 + 30%Fe- 5Ni-5N-17.5Si	-3.21	0.44	×	~	2.46 (25)	191 (10)	926(11)	35(1)	10.65	3.60 (23)	2.41 (15)	0	0	171.18 (1708)
G525-0S- 12.5Si	3	1600	70%ThB1 + 30%Fe- 5Ni-5N-12.5Si	-3.37	0.46	×	~	1.45 (12)	121 (3)	579(18)	39(4)	14.27 (44)	6.65	2.32 (15)	0	0	220.29 (1535)
G554-0S- 17.5Si	3	1800	70%ThB1 + 30%Fe- 5Ni-5N-17.5Si	-3.43	0.41	×		2.72 (29)	195 (14)	782(23)	28(3)	8.42	3.15 (22)	2.04 (15)	0	0	179.58 (1654)
G525-0S- 17.5Si	3	1600	70%ThB1 + 30%Fe- 5Ni-5N-17.5Si	-3.97	0.41	×		1.70 (11)	80(6)	477(9)	35(3)	9.90 (65)	3.38 (56)	2.84 (22)	0	0	189.28 (1423)
G526-10S- 17.5Si	2	1600	70%ThB1 + 30%Fe- 5Ni-5N-10S-17.5Si	-4.12	0.43	×		1.49	81(3)	456(7)	49(3)	19.23	8.90 (62)	0	0	0	294.63 (1821)
G525-10S- 17.5Si	3	1600	70%ThB1 + 30%Fe- 5Ni-5N-10S-17.5Si	-4.30	0.43	×	<b>/</b>	1.51 (7)	90 (14)	431(6)	25(6)	7.72 (56)	2.75 (51)	1.74 (21)	0	0	151.52 (1143)

The experiments in italics are from Grewal et al. (2019b), while the rest of experiments are from Grewal et al. (2019a)

Errors, reported in paranthesis, are 1- $\sigma$  error and are reported as the last digit cited. 927(18) should be read as 927  $\pm$  18 ppm.

<sup>&</sup>lt;sup>a</sup> For details see Table S2 in Grewal et al. (2019b) and Table 1 in Grewal et al. (2019a).

b  $fO_2$  with respect to iron-wüstite buffer (IW) is calculated using non-ideal solution model for both alloy and silicate melts. c NBO/T = (2 x Total O)/T - 4, where T = Si + Ti + Al + Cr + P.

<sup>&</sup>lt;sup>d</sup> 1-σ error is based on replicate EPMA analyses.

<sup>&</sup>lt;sup>e</sup> 1-σ error is based on replicate SIMS analyses.

f Bulk H content by FTIR is calculated using the Beer-Lambert Law at extinction coefficient 67 Lmol<sup>-1</sup>cm<sup>-1</sup> for water at ~3550 cm<sup>-1</sup>. See Supplementary Information for details.

g 1-σ error is based on propagated error for area under the fitted curve calculated from the FTIR data using the OriginPro software package.

#### 3.5. FTIR spectra

FTIR spectra were used to identify the structural interaction of dissolved C-O-N-H species in the silicate melt over the entire  $fO_2$  range ( $\sim$ IW - 4.2 to IW - 0.5). Fig. 2 shows the typical raw and background corrected, thickness normalized FTIR spectra of the experimental glasses across the entire  $fO_2$  range at a fixed P-T (3 GPa-1800 °C). FTIR spectra capture the presence of N-H, C-N, C-O, and O-H bonds in the silicate melt structure. Similar to Raman spectra, the intensity of the composite peak between  $\sim$ 3180 and 3370 cm $^{-1}$  increases with a decrease in  $fO_2$  till IW - 2.7, below which it drops with a further decrease in  $fO_2$ . Several other distinctive peaks lie at  $\sim$ 1420, 1530, 1610, 1730, 2120, and 2210 cm $^{-1}$ , whose intensities depend upon  $fO_2$ .

#### 4. DISCUSSION

# 4.1. Peak assignment for Raman spectra – comparison with previous studies and implications for volatile speciation in reduced silicate melts

In Fig. 1, the narrow asymmetric peak at  $\sim$ 2330 cm<sup>-1</sup> has been assigned to the main vibron of molecular N<sub>2</sub> (Roskosz et al., 2006). The identity of the peak found at  $\sim$ 2110 cm<sup>-1</sup> has been a source of debate. It has been assigned to the stretching vibration of C-O either in the form of isolated C-O molecules (Yoshioka et al., 2015), or Fe-carbonyl complexes (Wetzel et al., 2013). In contrast, Grewal et al. (2019b) argued that the higher C solubility in N-bearing silicate melts relative to N-free melts can be explained by the C-N- stretching vibron in Fe-cyanide complexes. However, due to the isoelectronic nature and therefore vibrational similarity between C-O and C-N<sup>-</sup>, as well as both of them being strong-field  $\pi$ -bonding ligands (Kettle et al., 2010; Barsan et al., 2011), the simultaneous presence of C-O and C-N stretching vibrations at  $\sim$ 2110 cm<sup>-1</sup> cannot be ruled out. The asymmetrical band at 2225 cm<sup>-1</sup>, attributed to Si-H stretching vibrations (Schmidt et al., 1998), was not detected in any of our samples.

The  $\sim$ 2920–2930 cm<sup>-1</sup> peak was assigned to the C-H stretching vibration of methane or methyl complexes (Murphy and Roberts, 1995; Mysen et al., 2009). The peaks  $\sim 3180 - 3190 \text{ cm}^{-1}$ ,  $\sim 3240 - 3250 \text{ cm}^{-1}$ ,  $\sim 3280 3290 \text{ cm}^{-1}$ , and  $\sim 3350-3370 \text{ cm}^{-1}$  were assigned to the stretching vibrations of N-H bonds in various N-H bearing molecules and complexes (Roskosz et al., 2006; Kadik et al., 2013). However, the exact identity of the N-H bearing species in this frequency range, i.e., NH<sup>2-</sup>, NH<sub>2</sub>, NH<sub>3</sub>, or NH<sup>+</sup>, has been a source of debate (Kadik et al., 2013: Dalou et al., 2019b; Mosenfelder et al., 2019). The broad asymmetric peak at ~3550-3580 cm<sup>-1</sup> which was assigned to the OH<sup>-</sup> stretching vibrations (Chi et al., 2014; Armstrong et al., 2015) can be observed in the most oxidized glasses ( $>\sim$ IW – 1.5). A band near 4130 cm<sup>-1</sup> assigned to the dissolution of molecular H2 (Schmidt et al., 1998; Hirschmann et al., 2012), was not detected in the Raman spectra of any of the samples.

# 4.2. Peak assignment for FTIR spectra – comparison with previous studies and implications for volatile speciation in reduced silicate melts

In the most oxidized experiments ( $log fO_2 > \sim IW - 1.1$ ) we see evidence for structurally bound  $CO_3^{2-}$  peaks with a characteristic doublet at  $1420-1430~\mathrm{cm}^{-1}$  and 1520-1530 cm<sup>-1</sup> (Fine and Stolper, 1985) (Fig. 2). The peak for molecular CO<sub>2</sub> at 2350 cm<sup>-1</sup> was not found in any of the samples. The 2205–2215 cm<sup>-1</sup> peak, observed at  $\log fO_2 > -$ IW - 2.0, was ascribed by Yoshioka et al. (2015) and Schmidt et al. (1998) to the dissolution of molecular C-O and Si-H stretching vibrations in the silicate melt structure, respectively. However, in this study we observed that the samples with 2205–2215 cm<sup>-1</sup> peak have a higher C/N ratio (Fig. 3A) relative to the reduced experiments at  $\log fO_2 < -$ IW - 2.0, where this peak is absent. Therefore, the assignment of 2205-2215 cm<sup>-1</sup> peak to C-N<sup>-</sup> vibrations in the silicate melt may explain the experiments at  $log fO_2 > -$ IW - 2.0 having a higher C/N ratio relative to the experiments at  $log fO_2 > IW - 2.0$ . The presence of C-N<sup>-</sup> species in a similar frequency range was also observed in the study of C-N bearing organic molecules (Socrates, 2001). Hence, the 2205–2215 cm<sup>-1</sup> peak could also belong to the simultaneous presence of triply bonded C-O and C-N<sup>-</sup> in the silicate melt. We report the first observation of a peak at  $2120-2135 \text{ cm}^{-1}$  at  $\sim \text{IW} - 3.0 \text{ to} - 1.7$ . The C/ N ratio of the silicate melts in this range is lower than the more oxidized experiments, which possibly contain C-N-(C:N = 1:1) bearing complexes, but is higher than the experiments at  $log fO_2 \le IW - 3.0$  (Fig. 3A). Therefore, the peak at 2120–2135 cm<sup>-1</sup> can possibly be explained by the C-N stretching band of  $^{-}N-C-N^{-}$  (C:N = 1:2) in carbodiimide complexes. Similar observations have been made in previous studies on organic and inorganic molecules (Socrates, 2001).

In contrast to previous studies with N-free systems, we find an additional peak at  $\sim 1730 \, \mathrm{cm}^{-1}$  below IW -2. Kadik et al. (2013) assigned this peak to the interactions of C-O with the silicate network. However, as fCO positively correlates with fO<sub>2</sub> (C + 1/2 O<sub>2</sub> = CO),  $\sim 1730 \, \mathrm{cm}^{-1}$  peak intensity area should not increase with a decrease in fO<sub>2</sub> if it belonged to the vibrations of isolated C-O molecules in the silicate network. Meanwhile, the  $\sim 1730 \, \mathrm{cm}^{-1}$  peak in organic molecules has been assigned to the stretching vibrations of C-O in complex groups like esters

to fCO, is also linked to  $fH_2$  which increases with a decrease in  $fO_2$  for  $H_2O$  bearing systems ( $H_2 + 1/2$   $O_2 = H_2O$ ). Therefore, an increase in  $\sim 1730 \, \mathrm{cm}^{-1}$  peak area with a decrease in  $fO_2$  can be explained by the possible formation of ester molecules.

The observed peak at 1605–1615 cm<sup>-1</sup> was ascribed by Kadik et al. (2013) to the deformational vibrations of molecular H<sub>2</sub>O, while Mosenfelder et al. (2019) assigned it to the in-plane bending motion of NH<sub>2</sub><sup>-</sup>, either in the

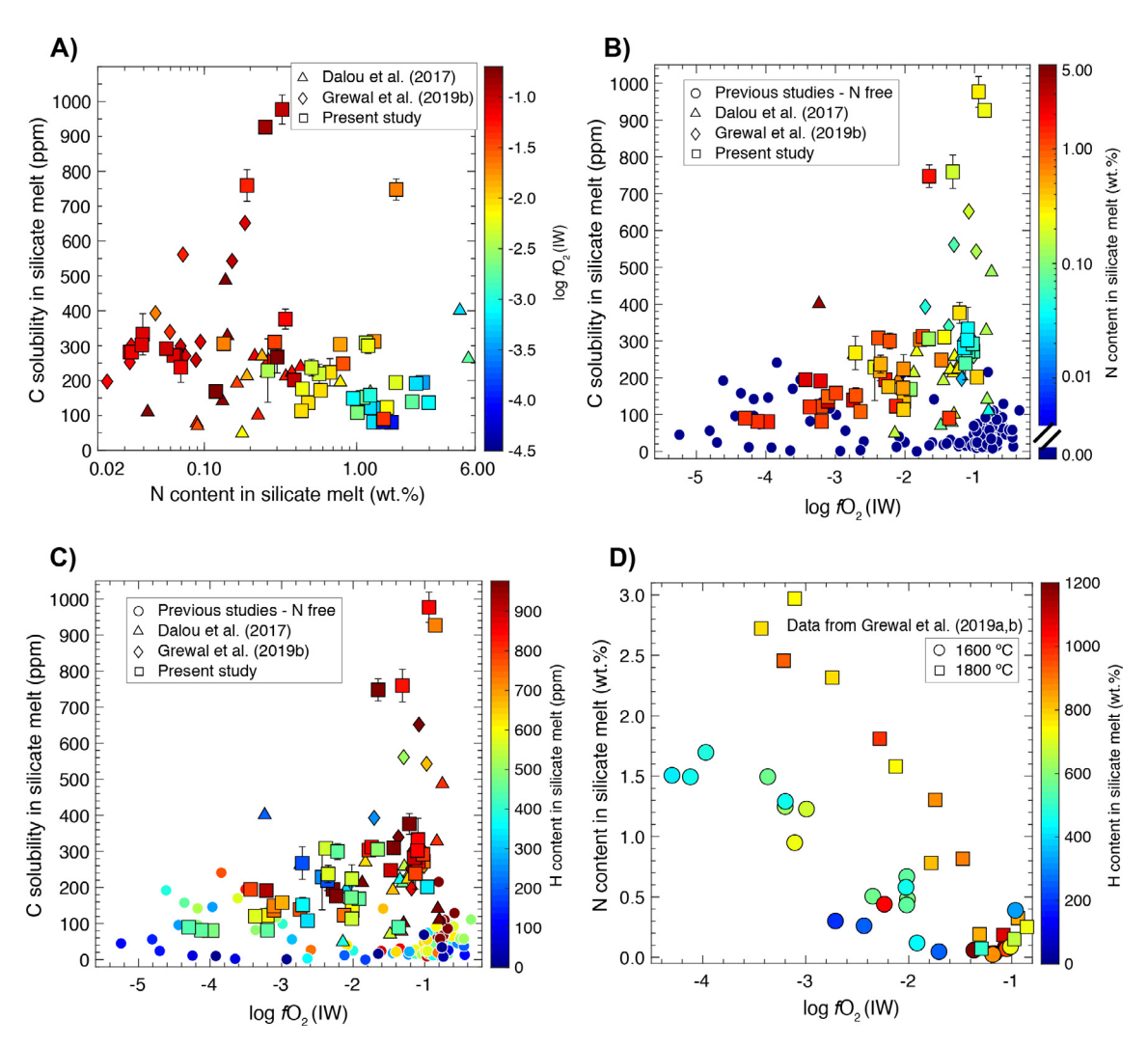


Fig. 3. C solubility in graphite saturated silicate melts as a function of: (A) and (B) N content and  $fO_2$ , and, (C)  $fO_2$  and H content. (D) N content in graphite saturated silicate melts as a function of  $fO_2$  and H content. Because previous studies on N partitioning between alloy and silicate melt did not target N solubility in the silicate melt, therefore, for comparison of N content in the silicate melt, data only from Grewal et al. (2019a,b) were plotted because of a fixed bulk N content in their starting mixes. Previous N-free studies: (Wetzel et al., 2013; Dasgupta et al., 2013; Stanley et al., 2014; Chi et al., 2014; Armstrong et al., 2015; Li et al., 2015; Li et al., 2016a; Duncan et al., 2017; Li et al., 2017; Tsuno et al., 2018). Error bars in A), B) and, C) represent  $\pm 1$ - $\sigma$  deviation based on the replicate ion probe analyses; where absent, the error bars are smaller than the symbol size.

form of primary amides (-CONH<sub>2</sub>) or primary amines (-NH<sub>2</sub>). The area under the curve for the 1605–1615 cm<sup>-1</sup> peak decreases with a decrease in  $fO_2$  (Fig. 2) but it does not show any correlation with bulk H bonded as OH. Therefore, the 1605–1615 cm<sup>-1</sup> peak should be related to N-H vibrations. In addition, area under the curve for the 1605–1615 cm<sup>-1</sup> range is higher at lower N content, where more H atoms are available to bond with each N atom relative to the more reduced conditions. However, C solubility in the silicate melt is also higher under relatively oxidized conditions; therefore, the 1605–1615 cm<sup>-1</sup> peak could belong to N-H vibrations in C-bearing primary amides (-CONH<sub>2</sub>) in addition to C-free primary amines (-NH<sub>2</sub>).

Another peak was found at  $1535-1545 \,\mathrm{cm}^{-1}$  (Fig. 2). In contrast to the  $1605-1615 \,\mathrm{cm}^{-1}$  peak, the area under the curve for the  $1535-1545 \,\mathrm{cm}^{-1}$  peak increases with a

decrease in  $fO_2$  (Fig. 2). As N content in the silicate melt increases with a decrease in  $fO_2$ , a smaller number of H atoms are available to bond with each dissolved N atom. Therefore, in agreement with Mosenfelder et al. (2019) we assign the 1535–1545 cm<sup>-1</sup> peak to the N-H vibrations in secondary amines (-NH).

Multiple peaks are found between  $\sim$ 3200 and 3380 cm<sup>-1</sup>. These peaks have been assigned to the presence of N-H complexes such as NH<sup>2-</sup>, NH<sub>2</sub>, NH<sub>3</sub>, and NH<sub>4</sub><sup>+</sup> by previous studies (Mysen et al., 2008; Mysen and Fogel, 2010; Kadik et al., 2013; Mosenfelder et al., 2019) but as discussed in the Raman spectroscopy section, the exact identity of these peaks remains uncertain. The wide asymmetric peak at  $\sim$ 3530 cm<sup>-1</sup> was assigned to the O-H stretching vibrations of chemically bound OH<sup>-</sup> (Stolper, 1982). As the asymmetric peak of the O-H vibron extends

over a wide range ( $\sim$ 2800–3800 cm<sup>-1</sup>), it interferes with N-H stretching frequency lying in a similar range. The deconvolution of the N-H stretching frequency signal from the O-H stretching frequency by setting asymmetric curved backgrounds is critical to determine the absolute strength of N-H peaks (Fig. 2A). This is necessary because under the most oxidized conditions ( $log fO_2$  between  $\sim IW - 2$  and IW - 1), where O-H peak intensity area is maximum, N-H peak intensity is most strongly affected by the overlap with the O-H peak (Fig. 2). If asymmetric curved backgrounds are not set to deduct the O-H vibration signal, then the apparent N-H peak area under the curve would seem to be the highest under the most oxidized conditions. However, this would be an erroneous conclusion because N-H peak intensity should increase with a decrease in fO<sub>2</sub> because fH<sub>2</sub> increases with a decrease in fO<sub>2</sub> at constant bulk H<sub>2</sub>O content in the silicate melt (Kadik et al., 2013; Kadik et al., 2017).

#### 4.3. C-O-N-H interactions in reduced silicate melts

Our data, in agreement with Grewal et al. (2019b), show that C solubility in the reduced silicate melts is higher in N-bearing systems (Dalou et al., 2017; Grewal et al., 2019b) compared to N-free systems (Dasgupta et al., 2013; Chi et al., 2014; Armstrong et al., 2015; Li et al., 2015; Wetzel et al., 2015; Li et al., 2016a; Li et al., 2017; Tsuno et al., 2018; Dasgupta and Grewal, 2019) at  $\log fO_2 > IW - 3$ , whereas it is similar in Nbearing and N-free systems at  $log fO_2 \le IW - 3$ (Fig. 3B). Additionally, while C solubility does not correlate with bulk H content at  $log fO_2 > IW - 3$ , it increases with bulk H at  $\log fO_2 < IW - 3$  (Fig. 3C). A similar increase in C solubility with increase in bulk H has been observed in N-free systems (Li et al., 2016a; Li et al., 2017), albeit starting at a somewhat higher  $fO_2$ , i.e.,  $log fO_2 \le IW - 1$ . At such reducing conditions, C-H is the dominant C species. N content in the silicate melt increases with a decrease in  $fO_2$  and increasing T (Dalou et al., 2017; Speelmanns et al., 2019; Grewal et al., 2019a). N content in the silicate melt also shows a positive correlation with bulk H content (Fig. 3D). However, bulk H content in Fig. 3D is generally greater at higher T which means it is not clear whether the effect of bulk H holds independent of T. Future work is necessary to validate this observation. C solubility positively correlates with N content in the silicate melt at  $\log fO_2 > IW - 1.5$ , but it drops off at  $\log fO_2 \le IW - 1.5$  even though there is a substantial increase in N content (Fig. 3A). This means that C-N complexation, as corroborated by FTIR and Raman spectra in this study, is an important factor in the dissolution of C and N in the silicate melt in relatively oxidized MOs. It also explains the higher C solubility in silicate melts in N-bearing systems relative to N-free systems under such conditions.

Although the experiments reported in Grewal et al. (2019b, 2019a) were conducted over a wide  $fO_2$  range (NBO/T = 0.4–2.2), the variation of NBO/T is coupled to the variation of  $fO_2$  (Fig. S3A), i.e., a decrease in  $fO_2$  leads to a decrease in NBO/T primarily due to the reaction:

 $Si_{(metal)} + FeO_{(silicate)} = Fe_{(metal)} + SiO_{2(silicate)}$ . Therefore, it is not possible to decouple the effect of  $fO_2$  from NBO/T such that the effect of NBO/T on C-O-N-H speciation can be constrained. Similarly, the effect of molar volume of silicate glasses on the C-O-N-H speciation cannot be predicted from our experimental results because molar volume is coupled to  $fO_2$  at a given P-T (Fig. S3B). Future experimental work is required to constrain the effect of silicate melt composition, i.e., NBO/T and molar volume, on C-O-N-H speciation.

To constrain the relative contribution of different C and N species as a function of  $fO_2$ , below, we discuss a subset of experiments at three different P-T conditions (3 GPa-1600 ° C, 3 GPa-1800 °C, and 4.5 GPa-1800 °C) over the entire fO<sub>2</sub> range. Fig. 4A shows that C solubility decreases exponentially with a decrease in fO<sub>2</sub> followed by a small increase at  $\sim$ IW – 3. At  $\sim$ IW – 1, C solubility in N-bearing systems positively correlates with P and T, while at  $<\sim$ IW – 1.5, it positively correlates with T with near P independence. At  $\sim IW - 1$ , C solubility positively correlates with N content (Fig. 3A,B). As N content in the silicate melt increases with an increase in P and T under oxidized conditions (Speelmanns et al., 2019; Grewal et al., 2019b; Grewal et al., 2019a), there are similar positive correlations of C solubility with P and T due to the presence of C≡N<sup>-</sup> complexes (Grewal et al., 2019b). Thickness normalized area under the curve for the  $\sim$ 2210 cm<sup>-1</sup> peak, assigned to C≡N<sup>-</sup> vibrations, manifests the positive effect of P and T on C solubility under oxidized conditions (Fig. 4B). The positive correlation between C solubility (at graphite saturation) and P under oxidized conditions observed in this study is in contrast with the anticorrelation known in N-free systems, where C is predominantly present as CO<sub>3</sub><sup>2-</sup>, at less than 4 GPa (Holloway et al., 1992; Hirschmann and Withers, 2008; Stanley et al., 2011; Dasgupta et al., 2013; Eguchi and Dasgupta, 2017; Eguchi and Dasgupta, 2018), but is in agreement with C solubility in N-free systems at a much higher P (10 GPa) where C solubility as high as 5200 ppm has been observed at  $\sim IW - 1.5$  under graphite saturated conditions (Malavergne et al., 2019).

Depending on the fO2, FTIR data shows the presence of C-O species like CO<sub>3</sub><sup>2-</sup> and CO in addition to C-N complexes. The  $\sim 1420 \text{ cm}^{-1}$  peak, assigned to  $CO_3^{2-}$  (e.g., Fine and Stolper, 1985; Brooker et al., 1999), is present only at  $>\sim$ IW – 1. Similar observations on the absence of CO<sub>2</sub><sup>2</sup> species at  $log fO_2 \le IW - 1$  have also been reported in previous studies in N-free systems (e.g., Li et al., 2015, 2016). The  $\sim$ 2130 cm<sup>-1</sup> peak shows a significant presence only at  $\log fO_2 \sim IW - 2$  (Fig. 4C). Although this peak has been previously assigned to the stretching vibration of C=O, its bonding environment is a source of debate. Wetzel et al. (2013) assigned this peak to C=O vibrations in Fecarbonyl, while Armstrong et al. (2015) and Yoshioka et al. (2015) suggested that this peak belonged to the interaction of isolated C=O molecules in the silicate network. Because  $\sim 2130 \text{ cm}^{-1}$  peak in this study is only present in silicate glasses which contain significant amounts of Fe (>4.5 wt.% FeO), Fe-carbonyl complexes could be the pri-

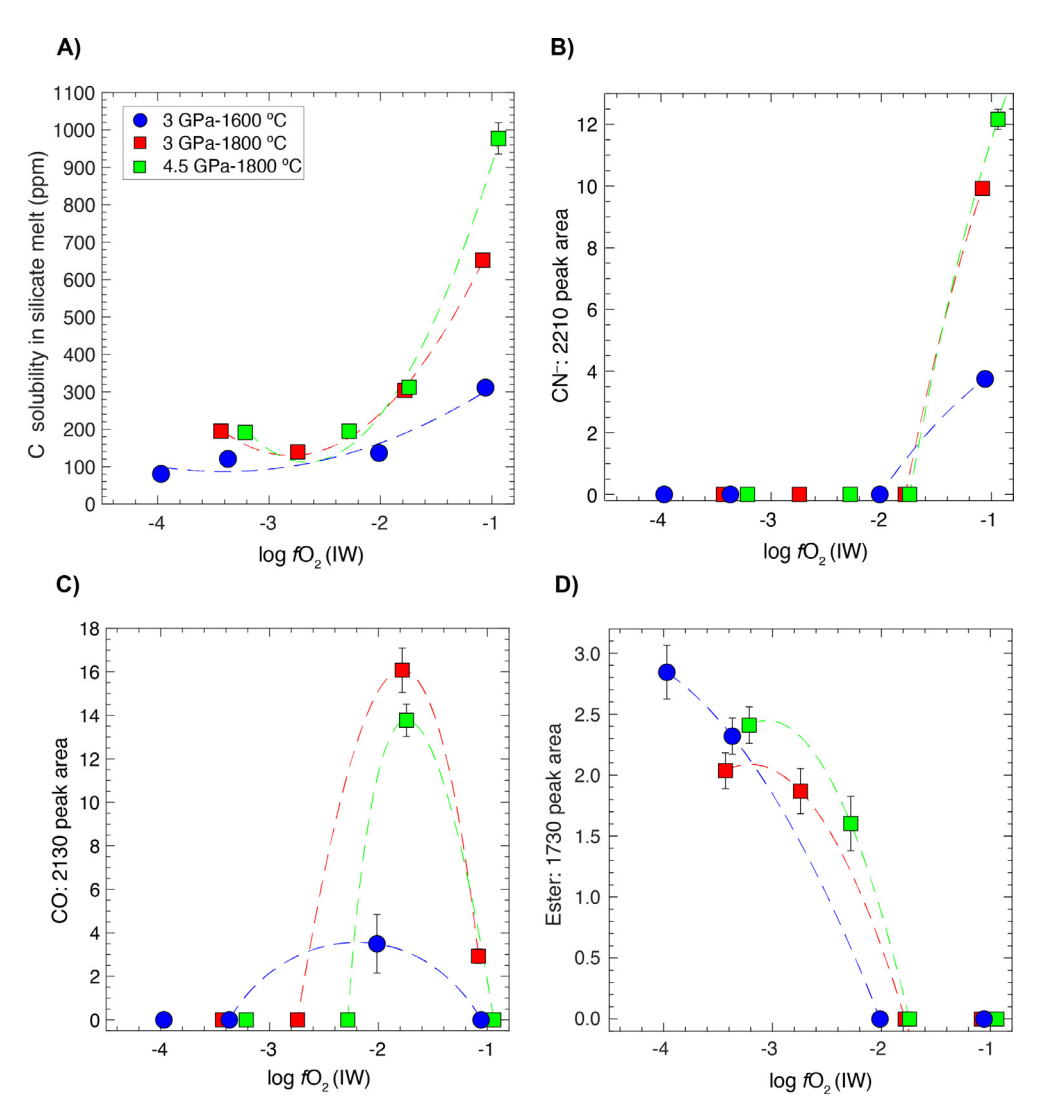


Fig. 4. (A) C solubility and thickness normalized peak areas of possible (B)  $CN^-$ , (C) CO, and (D) ester species as a function of  $fO_2$  at three different P-T. The dashed lines are best fitted curves that qualitatively track the trends at a fixed P-T. Error bars represent  $\pm 1$ - $\sigma$  deviation based on the replicate ion probe analyses (A) or propagated error for normalized area under the fitted curve calculated from the FTIR data (B, C, and D); where absent, the error bars are smaller than the symbol size.

mary carriers of C=O in the silicate network; however, a small contribution of isolated C≡O molecules cannot be ruled out. Additionally, an absence of  $\sim 2130 \text{ cm}^{-1}$  peak at  $\log fO_2 > IW - 1$  suggests that at under these conditions C dissolves mainly as  $CO_3^{2-}$  or  $C \equiv N^-$  complexes. The  $\sim$ 1730 cm<sup>-1</sup> peak area increases with a decrease in  $fO_2$ . Kadik et al. (2013) tentatively assigned this peak to the C=O vibrations in the silicate melt structure, but they could not identify the molecular structure of the species. fCO decreases with a decrease in fO2; therefore, the  $\sim$ 1730 cm<sup>-1</sup> peak cannot be assigned to the presence of isolated CO molecules. However, assignment of the  $\sim$ 1730 cm $^{-1}$  peak to ester molecules can simultaneously explain the presence of C=O vibrations as well as an increase of its peak area with a decrease in fO2 because of its co-dependence on both fH2 and fCO which increase and decrease with a decrease in  $fO_2$ , respectively.

To determine the relative importance of dissolution of C and N in the silicate melt as hydrogenated and nonhydrogenated species, it is crucial to ascertain the relative amounts of bulk H that is bonded as O-H and non-O-H species. H content determined by FTIR, which quantifies the amount of H bonded as O-H, was subtracted from the bulk H content determined using SIMS to yield the amount of H bonded as non-O-H species. Fig. 5 shows that the percentage of bulk H bonded as non-OH species increases exponentially from IW - 0.8 to IW - 4.5. At the most oxidized conditions the percentage of H bonded as non-OH species is  $\sim$ 60%, while at the most reduced conditions it is > 90%. It is important to note that in comparison to N-free systems (Li et al., 2015; Li et al., 2016a), N-bearing systems from this study have a higher amount of H present as non-OH species, primarily bonded as N-H, under oxidized conditions. However, the gap reduces

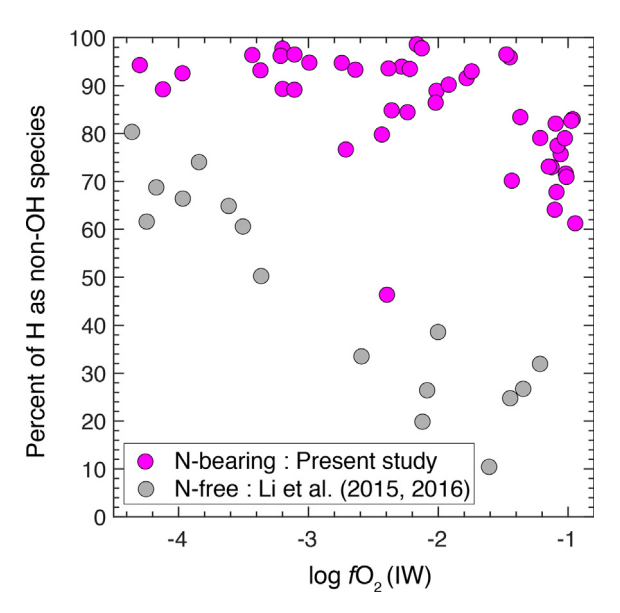


Fig. 5. Percentage of bulk H that is bonded as non-OH species like C-H and N-H as a function of  $fO_2$ . Percentage of H bonded as O-H decreases, while percentage of H bonded as non-O-H increases with a decrease in  $fO_2$ . N-bearing systems have higher amount of N present as non-OH species under oxidized conditions, while the gap reduces at increasingly reduced conditions. The amount of H content determined by FTIR, which quantifies the amount of H bonded as O-H in the silicate melt, was subtracted from the bulk H content determined using SIMS to yield the amount of H bonded as non-O-H species. The amount of H bonded as OH in the silicate glasses of this study and Li et al. (2016, 2015) was determined by using a fixed extinction coefficient of 67 Lmol $^{-1}$ cm $^{-1}$  for OH $^{-1}$  at  $\sim 3550$  cm $^{-1}$  (For details see Supplementary Information).

at increasingly reduced conditions which points towards the increase in the presence of C-H species in addition to N-H with lower  $fO_2$ .

N content in the silicate melt increases linearly with a decrease in logfO<sub>2</sub> (Fig. 6A). The possible mechanisms of N incorporation in the silicate melts under the reduced conditions prevalent during core-mantle differentiation and post-core formation stage in rocky bodies are: N<sub>2</sub>, N<sup>3-</sup>, NH<sup>2-</sup>, NH<sub>2</sub>, NH<sub>3</sub>, NH<sub>4</sub>, and CN<sup>-</sup> (Libourel et al., 2003; Mysen et al., 2008; Kadik et al., 2013; Armstrong et al., 2015; Dalou et al., 2019b; Mosenfelder et al., 2019; Grewal et al., 2019b). N is present in zero oxidation state in  $N_2$ , while all other species have N in -3 oxidation state, therefore, the interchange between N2 and all other reduced N species is controlled by fO2. The exact nature of interchange between hydrogenated N species, with variable degrees of hydration, and anhydrous N species would depend, however, on fH2 or the bulk H content in the system at a given  $fO_2$ .

N dissolution in the silicate melts under relatively oxidized conditions (>IW - 0.5) has been shown to follow Henry's Law, similar to the behavior of noble gases, with the locking of N<sub>2</sub> into the voids of the silicate melt structure (Miyazaki et al., 1995; Libourel et al., 2003). The value of Henry's constant of N<sub>2</sub> is comparable to that of Ar, owing to the similarity of size between N<sub>2</sub> and Ar (Miyazaki et al.,

1995; Libourel et al., 2003). The presence of the asymmetric  $\sim$ 2330 cm<sup>-1</sup> peak in the Raman spectra in the oxidized range ( $\sim$ IW - 2 to IW - 0.5) confirms dissolution of N in silicate melt as  $N_2$ .

The  $fO_2$  dependent chemical interaction of N with the silicate melt structure can be written as:

$$N_{2(g)} + 3H_2O_{(g)} = 2NH_{3(melt)} + 3/2O_{2(g)}$$
 (3)

$$O^{2-}_{(melt)} + N_{2(g)} + 2H_2O_{(g)} = 2NH_{2(melt)}^{-} + 3/2O_{2(g)}$$
 (4)

$$2O^{2-}_{(melt)} + N_{2(g)} + H_2O_{(g)} = 2NH^{2-}_{(melt)} + 3/2O_{2(g)}$$
 (5)

$$3O^{2-}_{(melt)} + N_{2(g)} = 2 N^{3-}_{(melt)} + 3/2O_{2(g)}$$
 (6)

It can be clearly seen from Eqs. (3)–(6) that at a given  $fN_2$ , the presence of N in the reduced form (-3 oxidation state) is favored as all reactions proceed to right at lower  $fO_2$ s. The degree of hydrogenation of the reduced N species positively correlates with  $fH_2$  which can be tracked by the following reaction:

$$H_2O_{(g)} = H_{2(g)} + 1/2O_{2(g)}$$
 (7)

There is no thermodynamic framework available to date to estimate fH<sub>2</sub> for complex C-O-N-H bearing fluids at elevated P-T. However, at a fixed P-T and assuming fixed  $a_{\rm H2O}$ ,  $f{\rm H}_2$  correlates with  $(f{\rm O}_2)^{-0.5}$ . This means that hydrogenated N species can be more easily formed under more reducing conditions at a given  $a_{\rm H2O}$ . However, the degree of hydrogenation of dissolved N species at a given P-T would depend on the comparison between  $fH_2$  and  $fN_2$ : 1) if  $fH_2$  is higher than  $fN_2$  under increasingly reduced conditions, then hydrogenated N species would be the dominant N species in the silicate melt structure; or 2) if fN<sub>2</sub> is higher than fH<sub>2</sub> under increasingly reduced conditions, then we should see a clear transition from hydrogenated N species being dominant in the less reduced end and nonhydrogenated N species would dominate on the highly reduced end of the spectrum.

Determining  $fN_2$  and  $fH_2$  for complex C-O-N-H bearing fluids is a non-trivial task. The available fluid composition model of Zhang and Duan (2009), which allows calculations of fugacity coefficients, chemical potentials, and P-V-T relationships is applicable for C-O-H systems with fluid species of H<sub>2</sub>O, CO<sub>2</sub>, CH<sub>4</sub>, H<sub>2</sub>, O<sub>2</sub>, CO, and C<sub>2</sub>H<sub>6</sub>. The equation of state developed for supercritical fluid mixture by Duan et al. (1992) also only considers  $N_2$  as the only possible N species. Therefore, employing the Zhang and Duan (2009) model to determine fCO or fH<sub>2</sub> as has been done for systems that contain significant concentration of N and likely species such as NH<sub>3</sub>, N<sub>2</sub>, and HCN (Armstrong et al., 2015; Dalou et al., 2019b) is expected to give erroneous results for fugacities of other species. Therefore, in the absence of estimates of fugacities of various gaseous species, we use N content in the silicate melt as a guide of  $fN_2$  because to a first-order approximation, N content in the silicate melt, which increases constantly with decrease in log fO<sub>2</sub>, tracks fN<sub>2</sub>. Similarly, bulk H content in the silicate melt bonded as non-OH can be used to track the available H content for N-H bonds and its effect on the degree of hydrogenation of N. Therefore, if the number of moles of H bonded as non-OH species is significantly

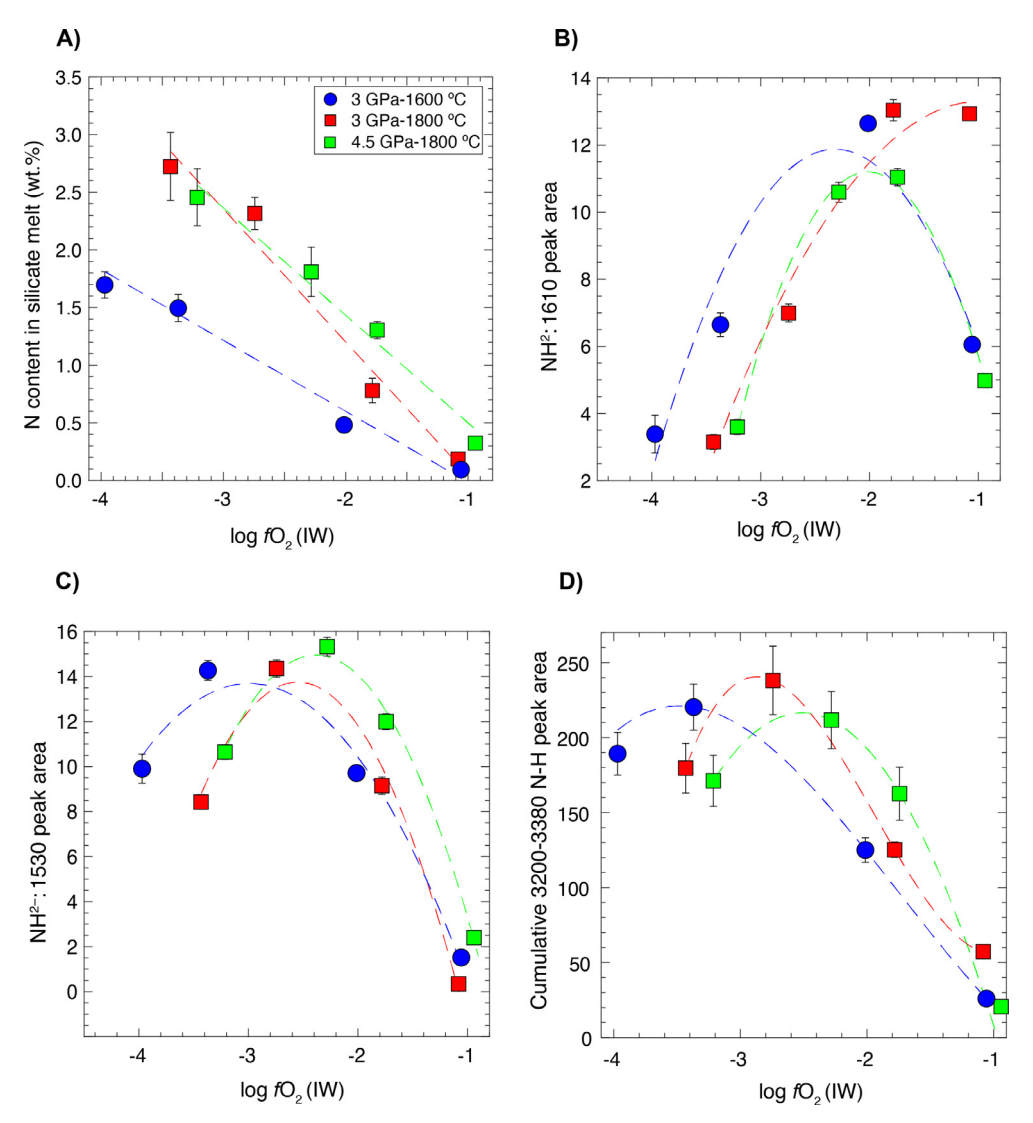


Fig. 6. (A) N content and thickness normalized peak areas representative of (B)  $NH_2^-$ , (C)  $NH^{2-}$  and (D) cumulative N-H as a function of  $fO_2$  at three different P-T conditions. The dashed lines are best fitted curves that qualitatively track the trends at a fixed P-T. Error bars represent  $\pm 1$ - $\sigma$  deviation based on the replicate electron microprobe analyses or propagated error for normalized area under the fitted curve calculated from the FTIR data; where absent, the error bars are smaller than the symbol size.

higher than the number of moles of N, then multiply hydrogenated N species would be the dominant N species in the silicate melt. On the other hand, if the number of moles of N is comparable to or higher than number of moles of H bonded as non-OH species, then monohydrogenated N species or anhydrous N species, respectively, would dominate the N speciation in the silicate melt.

Fig. 7 shows that the ratio of number of moles of N in the silicate melt to the number of moles of non-OH hydrogen species increases with a decrease in  $fO_2$ . At  $log/O_2 > -IW - 2$ , the ratio is less than 1, which means that hydrogenated reduced N species like  $NH^{2-}$ ,  $NH_2^-$ ,  $NH_3$ , and  $NH_4^+$ , could be dominant with little to no contribution from anhydrous  $N^{3-}$ . However, at  $log/O_2 < IW - 2$  the ratio is greater than 1, which means that the contribution of anhydrous  $N^{3-}$  starts to become important and at the most reduced end, i.e.  $log/O_2 < IW - 3$ , anhydrous  $N^{3-}$ 

would be the dominant N species with moderate contribution from hydrogenated N species. The FTIR data suggest the presence of NH<sup>2-</sup> and NH<sub>2</sub> peaks along with a possible absence of NH<sub>3</sub> and NH<sub>4</sub>. Normalized peak intensity area at ~1610 cm<sup>-1</sup>, assigned to NH<sub>2</sub> species, increases with decrease in  $\log fO_2$  from  $\sim IW - 1.0$  to  $\sim IW - 2.0$  and then again drops at more reduced conditions (Fig. 6B). In contrast, the ~1530 cm<sup>-1</sup> peak intensity area, assigned to NH<sup>2-</sup> species, attained its maximum contribution at more reduced conditions, i.e., between  $\sim IW - 2.5$  and -3.0(Fig. 6C). The normalized N-H peak intensity area  $(\sim 3200-3380 \text{ cm}^{-1})$ , which accounts for all possible N-H speciation, also shows a similar trend for all three sets of experiments (Fig. 6D). At  $\sim$ IW – 1.0, the N-H normalized area is at its minimum value due to low N content in the silicate melt and a significant contribution of other N species like  $N_2$  and  $CN^-$ . Between  $\sim IW - 1.0$  and  $\sim IW - 2.7$ , N-

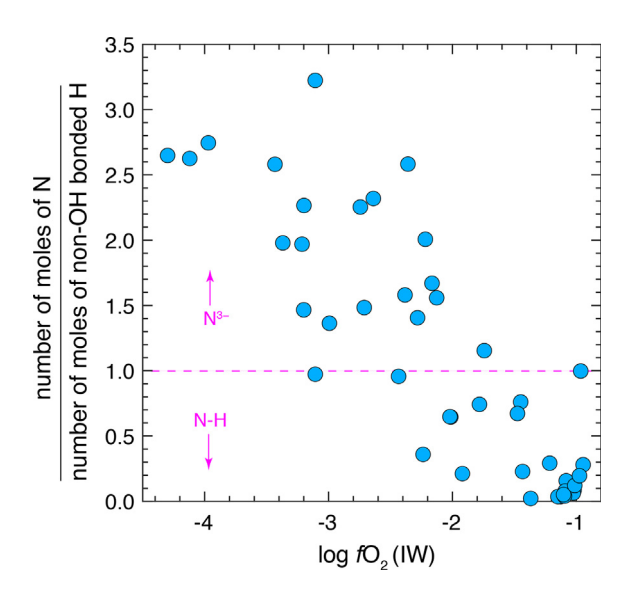


Fig. 7. Ratio of number of moles of N in the silicate melt to the number of moles of H bonded as non-OH species as a function of  $fO_2$  for all experimental data. As conditions become more reduced dissolution of N as anhydrous  $N^{3-}$  species becomes more prevalent, while hydrogenated N species (of -3 oxidation state) are dominant at more oxidizing conditions.

H peak intensity area increases, in parallel with an increase in N content, which means significant contribution of N-H bearing species like  $NH_2^-$  and  $NH^{2-}$  under such conditions. Below  $\sim IW-2.7$ , a significant increase in N content of the silicate melt despite a decrease in normalized N-H peak intensity area can only be explained by a major contribution by  $N^{3-}$  species along with some contribution from  $NH^{2-}$ .

We provide the first evidence for the effect of bulk H content on N dissolution in silicate melts. Several previous studies have predicted molecular NH<sub>3</sub> and/or ionic NH<sub>4</sub> to be the dominant N bearing species in the silicate melts that explains its high solubility under reduced conditions (Kadik et al., 2011; Kadik et al., 2013; Armstrong et al., 2015; Kadik et al., 2015; Kadik et al., 2017; Dalou et al., 2019b; Dalou et al., 2019a). However, our data suggests that Si-N linkages, either in the form of -Si-NH2 or -Si-NH-Si-, are the dominant N species in the silicate melts depending on bulk H content. Furthermore, we predict that the presence of H in the silicate melts is not a necessary condition to explain high N dissolution under reduced conditions. Anhydrous N<sup>3-</sup> linkages with Si should be the dominant N species as bulk H in the experimental silicate melts (e.g., Dalou et al., 2017; Grewal et al., 2019a) is not high enough to explain the high concentrations of N in silicate melts under highly reduced conditions. This conclusion is in agreement with high dissolution of N in reduced silicate melts under nominally anhydrous experimental conditions of Libourel et al. (2003).

## 4.4. Speciation of life-essential volatile elements in planetary magma oceans

Due to the variation in the redox conditions of their respective building blocks, rocky body differentiation in

the inner Solar System is postulated to have taken place across vastly different fO2s. Average fO2 during core formation for relatively smaller bodies is thought to have varied over several log units: Mercury: IW-5.5 (Zolotov et al., 2013); Mars: IW-1 (Rai and Van Westrenen, 2013); Vesta: IW-2 (Steenstra et al., 2016); Angrite parent body: IW-1.5 (Steenstra et al., 2017); and the Moon: IW-2 (Rai and Van Westrenen, 2014). Large planets like Earth had prolonged growth histories spread over tens of millions of years with initial growth from materials as reduced as IW-5 followed by gradual accretion of relatively oxidized material until the oxidation state of primitive upper mantle (IW-1.8) was attained (Rubie et al., 2011; Wade and Wood, 2005). Owing to their relatively short growth histories stretching for less than 5 Myr after the birth of the Solar System (Kleine et al., 2009), smaller rocky bodies would have formed only a single set of MO with relatively fixed proto-atmosphere compositions. On the other hand, large Earth-like planets could have formed several sets of MOs and degassed proto-atmospheres due to several stages of large-scale melting events during accretion and core formation, and the speciation of volatiles in MOs and compositions of those atmospheres would have differed significantly due to the variation in fO2 of the accreting material over several log units. In contrast to other rocky bodies in the inner Solar System (e.g., Mercury, Mars, the Moon) where the oxidation state of magmatic degassing throughout their history did not vary significantly from the oxidation state fixed by core-mantle equilibration (Wetzel et al., 2013; Li et al., 2017), the oxidation state of Hadean magmas on Earth evolved from  $\sim$ IW-2.0 to  $\sim$ IW + 3.0 within  $\sim$ 200 Ma of its formation (Trail et al., 2011).

Although the dissolved volatiles may undergo speciation change during degassing (Gaillard et al., 2011; Gaillard and Scaillet, 2014), the speciation of volatiles in MOs can still be used to deliver first-order predictions on the compositions of the proto-atmospheres (oxidized versus reduced) formed by MO degassing. To predict the compositions of the MOs and the resulting degassed proto-atmospheres applicable for rocky bodies in the inner Solar system at various stages of metal-silicate differentiation or shortly thereafter (Fig. 8), we divide our discussion into three different magma ocean conditions: (1) highly reduced MO – applicable for Mercury and early stage of Earth's accretion (~0–0.4 M<sub>E</sub>), (2) moderately reduced MO – applicable for Mars, the Moon, Vesta, Angrite Parent body and intermediate stage of Earth's accretion ( $\sim$ 0.4–0.8 M<sub>E</sub>), and (3) relatively oxidized MO – applicable for late stage of Earth's accretion ( $\sim$ 0.8–1  $M_{\rm E}$ ).

# 4.4.1. C-O-N-H volatile speciation in and above highly reduced MOs – Earth and Mercury

The accretion of Mercury and possibly the early stages of Earth's accretion (~0–0.4 M<sub>E</sub>) took place via accumulation of highly reduced, enstatite chondrite-like material (Wade and Wood, 2005; Rubie et al., 2011; McCoy and Nittler, 2014). Enstatite chondrites contain C and N exclusively in reduced, refractory phases like graphite, carbides and nitrides (Grady and Wright, 2003), which would result in most of their C and N budget surviving volatility related

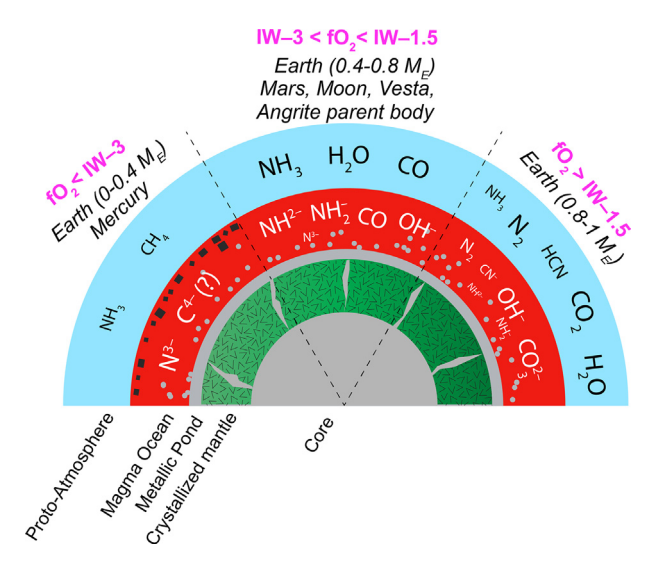


Fig. 8. Illustration showing the relative contribution of different C-O-N-H species in the MOs and their effect on the composition of the overlying proto-atmosphere formed by MO degassing in different rocky bodies in the inner Solar System. The sizes of different species/gases signify the proposed relative abundance of different species. Grey circles represent the metal droplets separating from the MO, while black rectangles represent floating graphite. The grey marks in the crystallized mantle represent the diapering metal to the core.

losses pre- and post-accretion. Therefore, the contribution of enstatite chondrite-like material to the C and N budget of the bulk silicate portions of the rocky bodies could be significant (Grewal et al., 2019a). Under these highly reduced conditions (<IW-3), C shows siderophile character  $(D_C^{\text{alloy/silicate}} = \sim 100-1000$ ; Li et al., 2015, 2016), while N a strongly lithophile element  $(D_N^{alloy/silicate} = \sim 0.001-0.1;$  Dalou et al., 2017; Grewal et al., 2019a). Spectroscopic data from this study shows that under highly reduced conditions dissolved C in the silicate melts was present as hydrogenated species (either as isolated hydrocarbon molecules or chemically combined with the silicate melt as Si-C-H linkages), while N was predominantly present as anhydrous N<sup>3-</sup> along with a significant contribution of N-H species (bonded with silicate network as Si-N or Si-N-H linkages, respectively). However, the earliest formed protoplanets could have been extremely waterpoor to water-free (e.g., Morbidelli et al., 2012; Alexander, 2017; Alexander et al., 2018), therefore, in contrast to many of the experiments containing weight percent level dissolved H<sub>2</sub>O equivalent, extensive formation of C-H and N-H species in highly reduced, anhydrous MOs may not be possible. Our experimental data under highly reduced, mildly hydrous conditions shows that anhydrous N<sup>3-</sup> is the dominant N bearing species in the silicate melts. Consequently, for highly reduced, nominally anhydrous MOs, N would be present mostly as anhydrous N3- by displacing tetrahedrally bonded O in the silicate network owing to the similarity of size between  $N^{3-}$  and  $O^{2-}$  (Baur, 1972). The storage of N<sup>3-</sup> as TiN has also been hypothesized under such reducing conditions (Libourel et al., 2003;

Speelmanns et al., 2019), but its presence cannot be ascertained from our study due to the TiO2-free nature of most of our starting mixes. Similarly, under truly anhydrous conditions, the dissolved C may be present as anhydrous C<sup>4-</sup> via Si-C linkages by displacing tetrahedrally bonded O in the silicate network (Sen et al., 2013). Future experimental studies in truly anhydrous conditions would be required to confirm the presence of anhydrous Si-C linkages in the silicate melt structure. Additionally, the low solubility of C in the silicate melt under highly reduced conditions (few tens of ppm) can also result in the saturation of C in the form of graphite (Holloway et al., 1992; Li et al., 2017; Keppler and Golabek, 2019). C saturation in the core and subsequent floatation of graphite in the MO has been postulated to explain the high C content on Mercury's surface (Peplowski et al., 2016) and has also been validated as a possibility through experiments (Li et al., 2016a). Similar saturation of N phases like Si<sub>3</sub>N<sub>4</sub> may not expected in MOs, except at final stages of MO crystallization, due to the extremely high solubility of N in highly reduced silicate melts (Libourel et al., 2003) as well as relatively low bulk N in the highly reduced building blocks (tens to few hundreds of ppm; Grady and Wright, 2003).

The presence of C as graphite along with locking of C and N in tetrahedrally bonded sites in the silicate melts with anhydrous Si-C and Si-N linkages would mean that in highly reduced, anhydrous MOs a significant amount of the C-N budget can be retained in the MO without significant degassing into the atmosphere. Solubility in the order of 100–1000 s of ppm in highly reduced, anhydrous silicate melts at 1 bar (Libourel et al., 2003) confirms that a significant proportion of N budget in such MOs can be retained in the silicate reservoirs. Therefore, after core formation, significant amounts of C and N can reside in the silicate portions of rocky planets under anhydrous conditions. However, the presence of small amounts of H<sub>2</sub>O, analogous to the results of experimental studies, would lead to N-H and C-H being the dominant N and C species in the silicate melt, respectively. Release of N-H and C-H species as CH<sub>4</sub> and NH<sub>3</sub> due to magma degassing could have led to the formation of reducing atmospheres.

4.4.2. C-O-N-H volatile speciation in and above moderately reduced MOs – Earth, the Moon, Mars, Vesta, and Angrite parent body

The intermediate stage accretion of Earth ( $\sim$ 0.4–0.8  $M_{\rm E}$ ) possibly proceeded by an admixture of reduced material similar to enstatite chondrites and some contribution from relatively oxidized material similar to ordinary chondrites (Wade and Wood, 2005). Between IW–3 to IW–1.5, i.e., at intermediate stage to end of core formation or young post-core formation MO, C shows highly siderophile character ( $D_{\rm C}^{\rm alloy/silicate} = \sim 100-10,000$ ; Li et al., 2015, 2016), whereas N acts as a mildly lithophile to mildly siderophile element ( $D_{\rm N}^{\rm alloy/silicate} = \sim 0.1-10$ ; Dalou et al., 2017; Grewal et al., 2019a; Speelmanns et al., 2019). Spectroscopic data from our study shows that CO is the major C bearing species, and N-H speciation either in the form of NH<sup>2-</sup> or NH<sub>2</sub><sup>-</sup> dominates the N speciation in the silicate melt. CO can be dissolved in the form of Fe-carbonyls

(Wetzel et al., 2013) or molecular CO (Yoshioka et al., 2015) or complex molecules like esters. NH<sup>2-</sup> or NH<sub>2</sub><sup>-</sup> dissolution takes place by the replacement of non-bonding oxygen from the silicate network (Mysen et al., 2008). C-H bearing molecules along with anhydrous N<sup>3-</sup> would be the minor C and N species, respectively, along with a minor contribution from C-N bearing carbodiimide complexes. Additionally, if the bulk H content of the silicate melt is much higher than the bulk N content, then H would also be present in the form of OH<sup>-</sup> in the silicate melt in addition to N-H or C-H bearing species. As C and N are not locked in the non-bridging sites of the silicate network, early terrestrial atmospheres formed by MO degassing during these conditions could have led to the formation of reducing CO and NH<sub>3</sub>-rich atmospheres along with the presence of water vapor. Formation of such atmospheres would also be predicted for the MO degassing of Mars, the Moon, Vesta, and the angrite parent body. However, due to their small gravity, Vesta, angrite parent body, and the Moon would not have retained these MO degassed atmospheres (Odert et al., 2018), thus reduced atmospheres would not likely have played a part in their planetary evolution. Retention of NH3-bearing reduced MO degassed proto-atmospheres for a few hundred million years on Mars could provide an alternate explanation to the faint young Sun paradox and the subsequent stability of liquid water on Martian surface early on in its history (Sagan and Mullen, 1972; Sagan and Chyba, 1997).

### 4.4.3. C-O-N-H volatile speciation in and above relatively oxidized MOs-Earth

Final stages of Earth's accretion and core formation (~0.8–1 M<sub>E</sub>) could have proceeded with a significant contribution from the most oxidized and volatile-rich building blocks, i.e., carbonaceous chondrites. Although carbonaceous chondrites, especially CI chondrites, are extremely volatile rich (as high as ~5 wt.% C, ~5000 ppm N and ~10 wt.% H<sub>2</sub>O; Alexander et al., 2012), they contain volatiles in thermally unstable phases like insoluble organic matter (IOM), which would make them susceptible to high degrees of volatile loss during the impact related delivery process (Speelmanns et al., 2019; Grewal et al., 2019a). However, owing to the relatively large volatile inventories, some amount of their delivered volatiles would have been retained in MOs, either by direct incorporation or via ingassing from the volatiles released to the atmosphere on delivery. Under these oxidizing conditions, i.e., log fO<sub>2</sub> above IW-1.5, C-N bearing cyanide complexes, CO<sub>3</sub><sup>2-</sup>, N<sub>2</sub>, NH<sup>2-</sup>, NH<sub>2</sub> and OH<sup>-</sup> would be the dominant C-O-N-H bearing species dissolved in the silicate melt. Although the relative contribution of C-N bearing molecules would not be as high as predicted by the experimental data from this study owing to the relatively high bulk N content in the system, the presence of HCN and NH<sub>3</sub> in even small quantities in the MO degassed proto-atmospheres could have played an extremely important role in the production of organic molecules (Chyba and Sagan, 1992). Retention of these atmospheres which are predisposed for abiotic organic synthesis could have resulted in the origins of life on our planet (Sagan and Mullen, 1972).

#### 4.5. The effect of volatile dissolution in silicate melts on alloysilicate fractionation of nitrogen and carbon

Several high P-T experimental studies have recently determined elemental partitioning of N and C between core-forming alloy melt and equilibrium silicate melt, i.e.,  $D_N^{alloy/silicate}$  (Roskosz et al., 2013; Li et al., 2016b; Dalou et al., 2017; Speelmanns et al., 2019; Grewal et al., 2019b; Grewal et al., 2019a) and D<sub>C</sub> alloy/silicate (Dasgupta et al., 2013; Chi et al., 2014; Li et al., 2015; Li et al., 2016a; Dalou et al., 2017; Tsuno et al., 2018; Malavergne et al., 2019; Grewal et al., 2019b), respectively. Although the main goal of these studies was to constrain alloy-silicate partitioning of C and/or N in magma ocean-relevant conditions, all experimental systems were variably hydrous. In particular, dissolved H content in the quenched glasses in this study and relevant previous studies, expressed as H2O, varied between 0.01 and 2.14 wt.%. Therefore, the determined  $D_N^{\text{alloy/silicate}}$  and  $D_C^{\text{alloy/silicate}}$  could be affected by hydrogenated N or C species in the silicate melt and these datasets are chiefly applicable for hydrous MO settings; the direct application of experimentally determined  $D_{\scriptscriptstyle N}^{\text{alloy/silicate}}$ and D<sub>C</sub> alloy/silicate to an anhydrous MOs may be problematic. As all protoplanetary bodies in the inner Solar System were likely water-poor (Morbidelli et al., 2012; Alexander, 2017; Alexander et al., 2018), terrestrial MOs could have been extremely water-poor to water-free if water was primarily delivered during the last stages of their accretion (Albarède, 2009; Morbidelli et al., 2012; Dauphas and Morbidelli, 2014).

Previous studies have shown that  $D_N^{\text{alloy/silicate}}$  continuously drops with a decrease in fO2 and N shows increasingly lithophile character under highly reduced conditions (<IW-2; Dalou et al., 2017; Speelmanns et al., 2019; Grewal et al., 2019a). This observation has been explained by the N-H being the predominant N bearing species under reduced conditions by Dalou et al. (2017). However, based on our data we infer that even under nominally hydrous conditions of our experiments, N<sup>3-</sup> is the dominant N bearing species in the silicate melts (Fig. 7). Therefore, enhanced dissolution of N in silicate melt with decreasing fO<sub>2</sub> is not reliant entirely upon  $fH_2$  and the experimentally determined increasingly lithophile character of N should be still applicable for nominally anhydrous MOs as long as the MOs are graphite saturated. If this is true, then the reasoning for the surprisingly large N isotopic fractionation between alloy and silicate reservoirs during core-mantle differentiation determined by Dalou et al. (2019a), contrary to all theoretical calculations (Young et al., 2015; Bourdon et al., 2018) and a previous experimental study (Li et al., 2016b), needs to be re-visited as their calculations are based on the assumption that N-H is the predominant N bearing species in their experiments under increasingly reduced conditions.

In N-free systems,  $D_C^{alloy/silicate}$  is shown to increase with a decrease in  $fO_2$  due to a drop in C solubility in the silicate melts as  $CO_3^{2-}$  and CO abundance decreases (Holloway et al., 1992; Dasgupta et al., 2013; Chi et al., 2014). How-

ever, under increasingly reduced conditions (<IW-1.5), D<sub>C</sub> alloy/silicate decreases primarily due to an increase in C solubility owing to the dissolution of C as C-H (Li et al., 2015; Li et al., 2016a; Li et al., 2017). A similar turnover of C solubility in the silicate melt was also observed in the Nbearing system of this study, albeit at even more reduced conditions (<IW-3; Fig. 4A). However, if reduced MOs are anhydrous, then C-H species would not form and D<sup>alloy/silicate</sup> should be expected to continue to increase with a decrease in fO<sub>2</sub> as predicted by Chi et al. (2014). Therefore, under highly reduced conditions for anhydrous MOs, the siderophile character of C could be even higher than previously predicted (Li et al., 2015; Li et al., 2016a). In other words, anhydrous MOs, which are highly reduced (e.g., logfO<sub>2</sub> < IW-3) may observe even greater fractionation of C and N during core formation at graphite saturated conditions. Future studies, however, need to constrain whether anhydrous C<sup>4-</sup> species can become stable in anhydrous, reduced MO, which could suppress the expected fractionation of C/N during core formation.

#### 5. CONCLUDING REMARKS

Using SIMS, Raman, and FTIR analysis of experimental silicate glasses, we show that C-O-N-H dissolution in the silicate melts over a wide range of P-T-fO<sub>2</sub>-NBO/T is strongly controlled by fO<sub>2</sub>. Under relatively oxidizing conditions (>IW-1.5), mixed volatile speciation of C≡N<sup>-</sup>, prevalent at more reducing conditions (between IW-3 to IW-1.5). At the most reducing conditions (<IW-3) N is locked in the silicate network as anhydrous N<sup>3-</sup> linkages. Similar C locking in the silicate network as C4- may also be possible under truly anhydrous conditions but needs to be verified by future investigations. Therefore, in highly reduced and anhydrous MOs, C and N may reside in the silicate reservoirs as non-volatile species like  $C^{4-}$  and  $N^{3-}$  in addition to the presence of refractory C and N saturated phases like graphite and Si<sub>3</sub>N<sub>4</sub>, respectively. It is important to note that all experimental data on C-O-N-H speciation in silicate glasses in this study and previous studies was under graphite saturated conditions in basaltic to andesitic silicate melts. As typical MOs are expected to be graphite undersaturated with ultramafic silicate melts, future experimental effort would be required to determine whether C-O-N-H speciation in silicate glasses under such conditions corroborates previous work. Additionally, MOs are transient stages in rocky body evolution with each MO stage stretching over few hundreds to thousands of years followed by solidification of the silicate reservoirs (Elkins-Tanton, 2012). Whether C and N incorporate into the solid silicate reservoirs of rocky bodies post MO crystallization in a similar fashion to the molten silicate melts is a largely unknown owing to lack of constraints on partitioning of C and N between solids and melts at  $\log fO_2 \le IW$ . If C, N, and H<sub>2</sub>O are incompatible in mantle minerals, the residual silicate liquid becomes enriched in these volatiles as the solidification progresses, which in turn would control the mass as well as the composition of the degassed atmosphere depending upon their solubilities in the residual melts. Therefore, future experimental work on phase relations and solid-melt partitioning at  $\log fO_2 < IW$  would be critical to constrain the fate of C-O-N-H post-MO crystallization.

#### **Declaration of Competing Interest**

The authors declare that they have no known competing financial interests or personal relationships that could have appeared to influence the work reported in this paper.

#### ACKNOWLEDGMENTS

The authors thank Brian Monteleone for his help with the ion probe analyses and James Eguchi for insightful discussions. Chris Herd is thanked for his comments and efficient handling of the manuscript. Three anonymous reviewers are thanked for their extremely thorough reviews, which helped to improve our communication. D.S.G was supported by a Lodieska Stockbridge Vaughn Fellowship by Rice University and a NASA FINESST grant 80NSSC19K1538 during the final preparation of this manuscript. NASA grants 80NSSC18K0828 and 80NSSC18K1314 to R.D. supported the work.

#### APPENDIX A. SUPPLEMENTARY MATERIAL

Supplementary data to this article can be found online at https://doi.org/10.1016/j.gca.2020.04.023.

#### REFERENCES

Albarède F. (2009) Volatile accretion history of the terrestrial planets and dynamic implications. *Nature* **461**, 1227–1233.

Alexander C. M. O. (2017) The origin of inner Solar System water. Philos. Trans. R. Soc. A Math. Phys. Eng. Sci. 375, 20150384.

Alexander C. M. O., Bowden R., Fogel M. L., Howard K. T., Herd C. D. K. and Nittler L. R. (2012) The provenances of asteroids, and their contributions to the volatile inventories of the terrestrial planets. *Science* 337, 721–723.

Alexander C. M. O., McKeegan K. D. and Altwegg K. (2018) Water Reservoirs in Small Planetary Bodies: Meteorites, Asteroids, and Comets. Space Sci. Rev. 214, 36.

Ardia P., Hirschmann M. M., Withers A. C. and Stanley B. D. (2013) Solubility of CH<sub>4</sub> in a synthetic basaltic melt, with applications to atmosphere-magma ocean-core partitioning of volatiles and to the evolution of the Martian atmosphere. Geochim. Cosmochim. Acta 114, 52–71.

Armstrong L. S., Hirschmann M. M., Stanley B. D., Falksen E. G. and Jacobsen S. D. (2015) Speciation and solubility of reduced C-O-H-N volatiles in mafic melt: implications for volcanism, atmospheric evolution, and deep volatile cycles in the terrestrial planets. *Geochim. Cosmochim. Acta* 171, 283–302.

Barsan M. M., Butler I. S., Fitzpatrick J. and Gilson D. F. R. (2011) High-pressure studies of the micro-Raman spectra of iron cyanide complexes: prussian blue (Fe<sub>4</sub>[Fe(CN)<sub>6</sub>]<sub>3</sub>), potassium ferricyanide (K<sub>6</sub>[Fe(CN)<sub>3</sub>]), and sodium nitroprusside (Na<sub>3</sub>[Fe(CN)<sub>5</sub>]). *J. Raman Spectrosc.* **42**, 1820–1824.

Baur W. H. (1972) Occurrence of nitride nitrogen in silicate minerals. *Nature* 240, 461–462.

- Bourdon B., Roskosz M. and Hin R. C. (2018) Isotope tracers of core formation. *Earth-Science Rev.* **181**, 61–81.
- Brearley A. J. (2006) The action of water. In Meteorites and the early Solar System II (eds DS Lauretta, HY McSween Jr). In Tucson, AZ: University of Arizona Press. pp. 584–624.
- Brooker R. A., Kohn S. C., Holloway J. R., McMillan P. F. and Carroll M. R. (1999) Solubility, speciation and dissolution mechanisms for CO<sub>2</sub> in melts on the NaAlO<sub>2</sub>-SiO<sub>2</sub> join. *Geochim. Cosmochim. Acta* **63**, 3549–3565.
- Chi H., Dasgupta R., Duncan M. S. and Shimizu N. (2014) Partitioning of carbon between Fe-rich alloy melt and silicate melt in a magma ocean – implications for the abundance and origin of volatiles in Earth, Mars, and the Moon. *Geochim. Cosmochim. Acta* 139, 447–471.
- Chyba C. and Sagan C. (1992) Endogenous production, exogenous delivery and impact-shock synthesis of organic molecules: an inventory for the origins of life. *Nature* **355**, 125–132.
- Dalou C., Füri E., Deligny C., Piani L., Caumon M.-C., Laumonier M., Boulliung J. and Edén M. (2019a) Redox control on nitrogen isotope fractionation during planetary core formation. *Proc. Natl. Acad. Sci.* 116, 14485–14494.
- Dalou C., Hirschmann M. M., von der Handt A., Mosenfelder J. and Armstrong L. S. (2017) Nitrogen and carbon fractionation during core-mantle differentiation at shallow depth. *Earth Planet. Sci. Lett.* 458, 141–151.
- Dalou C., Hirschmann M. M., Jacobsen S. D. and Le Losq C. (2019b) Raman spectroscopy study of C-O-H-N speciation in reduced basaltic glasses: implications for reduced planetary mantles. *Geochim. Cosmochim. Acta* 265, 32–47.
- Dasgupta R., Chi H., Shimizu N., Buono A. S. and Walker D. (2013) Carbon solution and partitioning between metallic and silicate melts in a shallow magma ocean: implications for the origin and distribution of terrestrial carbon. *Geochim. Cos-mochim. Acta* 102, 191–212.
- Dasgupta R. and Grewal D. S. (2019) Origin and Early Differentiation of Carbon and Associated Life-Essential Volatile Elements on Earth. Deep Carbon In Orcutt, B., Daniel, I., and Dasgupta, R. (Eds.) Deep Carbon: Past to Present. Cambridge Univ. Press. Cambridge, pp. 4–39.
- Dauphas N. and Morbidelli A. (2014) Geochemical and Planetary Dynamical Views on the Origin of Earth's Atmosphere and Oceans. Treatise on Geochemistry Elsevier, pp. 1–35.
- Duan Z., Møller N. and Weare J. H. (1992) Molecular dynamics simulation of PVT properties of geological fluids and a general equation of state of nonpolar and weakly polar gases up to 2000 K and 20,000 bar. *Geochim. Cosmochim. Acta* 56, 3839–3845.
- Duncan M. S., Dasgupta R. and Tsuno K. (2017) Experimental determination of CO<sub>2</sub> content at graphite saturation along a natural basalt-peridotite melt join: implications for the fate of carbon in terrestrial magma oceans. *Earth Planet. Sci. Lett.* 466, 115–128.
- Eguchi J. and Dasgupta R. (2018) A CO<sub>2</sub> solubility model for silicate melts from fluid saturation to graphite or diamond saturation. *Chem. Geol.* **487**, 23–38.
- Eguchi J. and Dasgupta R. (2017) CO<sub>2</sub> content of andesitic melts at graphite-saturated upper mantle conditions with implications for redox state of oceanic basalt source regions and remobilization of reduced carbon from subducted eclogite. *Contrib. to Mineral. Petrol.* 172, 12.
- Elkins-Tanton L. T. (2012) Magma oceans in the inner solar system. *Annu. Rev. Earth Planet. Sci.* 40, 113–139.
- Fine G. and Stolper E. (1985) The speciation of carbon dioxide in sodium aluminosilicate glasses. *Contrib. to Mineral. Petrol.* **91**, 105–121.
- Gaillard F. and Scaillet B. (2014) A theoretical framework for volcanic degassing chemistry in a comparative planetology

- perspective and implications for planetary atmospheres. *Earth Planet. Sci. Lett.* **403**, 307–316.
- Gaillard F., Scaillet B. and Arndt N. T. (2011) Atmospheric oxygenation caused by a change in volcanic degassing pressure. *Nature* 478, 229–232.
- Grady M. M. and Wright I. P. (2003) Elemental and isotopic abundances of carbon and nitrogen in meteorites. *Space Sci. Rev.* **106**, 231–248.
- Grewal D. S., Dasgupta R., Holmes A. K., Costin G., Li Y. and Tsuno K. (2019a) The fate of nitrogen during core-mantle separation on Earth. *Geochim. Cosmochim. Acta* 251, 87–115.
- Grewal D. S., Dasgupta R., Sun C., Tsuno K. and Costin G. (2019b) Delivery of carbon, nitrogen, and sulfur to the silicate Earth by a giant impact. *Sci. Adv.* 5, eaau3669.
- Hirschmann M. M. (2012) Magma ocean influence on early atmosphere mass and composition. *Earth Planet. Sci. Lett.* **341**–**344**, 48–57.
- Hirschmann M. M. and Withers A. C. (2008) Ventilation of CO2 from a reduced mantle and consequences for the early Martian greenhouse. *Earth Planet. Sci. Lett.* 270, 147–155.
- Hirschmann M. M., Withers A. C., Ardia P. and Foley N. T. (2012) Solubility of molecular hydrogen in silicate melts and consequences for volatile evolution of terrestrial planets. *Earth Planet. Sci. Lett.* 345–348, 38–48.
- Holloway J. R., Pan V. and Gudmundsson G. (1992) Highpressure fluid-absent melting experiments in the presence of graphite: oxygen fugacity, ferric/ferrous ratio and dissolved CO<sub>2</sub>. Eur. J. Mineral. 4, 105–114.
- Holzheid A., Palme H. and Chakraborty S. (1997) The activities of NiO, CoO and FeO in silicate melts. *Chem. Geol.* **139**, 21–38.
- Jarosewich E. (1990) Chemical analyses of meteorites: a compilation of stony and iron meteorite analyses. *Meteoritics* 25, 323–337.
- Kadik A. A., Koltashev V. V., Kryukova E. B., Plotnichenko V. G., Tsekhonya T. I. and Kononkova N. N. (2015) Solubility of nitrogen, carbon, and hydrogen in FeO-Na<sub>2</sub>O-Al<sub>2</sub>O<sub>3</sub>-SiO<sub>2</sub> melt and liquid iron alloy: influence of oxygen fugacity. *Geochemistry Int.* 53, 849–868.
- Kadik A. A., Kurovskaya N. A., Ignat'ev Y. A., Kononkova N. N., Koltashev V. V. and Plotnichenko V. G. (2011) Influence of oxygen fugacity on the solubility of nitrogen, carbon, and hydrogen in FeO-Na<sub>2</sub>O-SiO<sub>2</sub>-Al<sub>2</sub>O<sub>3</sub> melts in equilibrium with metallic iron at 1.5 GPa and 1400°C. Geochemistry Int. 49, 429–438
- Kadik A. A., Kurovskaya N. A., Lukanin O. A., Ignat'ev Y. A., Koltashev V. V., Kryukova E. B., Plotnichenko V. G. and Kononkova N. N. (2017) Formation of N-C-O-H molecules and complexes in the basalt-basaltic andesite melts at 1.5 Gpa and 1400°C in the presence of liquid iron alloys. *Geochemistry Int.* 55, 151–162.
- Kadik A. A., Litvin Y. A., Koltashev V. V., Kryukova E. B., Plotnichenko V. G., Tsekhonya T. I. and Kononkova N. N. (2013) Solution behavior of reduced N-H–O volatiles in FeO–Na<sub>2</sub>O–SiO<sub>2</sub>–Al<sub>2</sub>O<sub>3</sub> melt equilibrated with molten Fe alloy at high pressure and temperature. *Phys. Earth Planet. Inter.* 214, 14–24.
- Keppler H. and Golabek G. (2019) Graphite floatation on a magma ocean and the fate of carbon during core formation. *Geochem. Perspect. Lett.* **11**, 12–17.
- Kettle S. F. A., Diana E., Marchese E. M. C., Boccaleri E., Croce G., Sheng T. and Stanghellini P. L. (2010) The vibrational spectra of the cyanide ligand revisited: double bridging cyanides. *Eur. J. Inorg. Chem.* 2010, 3920–3929.
- King P. L., Vennemann T. W., Holloway J. R., Hervig R. L., Lowenstern J. B. and Forneris J. F. (2002) Analytical techniques for volatiles: a case study using intermediate (andesitic) glasses. *Am. Mineral.* 87, 1077–1089.

- Kleine T., Touboul M., Bourdon B., Nimmo F., Mezger K., Palme H., Jacobsen S. B., Yin Q. Z. and Halliday A. N. (2009) Hf-W chronology of the accretion and early evolution of asteroids and terrestrial planets. *Geochim. Cosmochim. Acta* 73, 5150– 5188.
- Li Y., Dasgupta R. and Tsuno K. (2017) Carbon contents in reduced basalts at graphite saturation: implications for the degassing of Mars, Mercury, and the Moon. *J. Geophys. Res. Planets* **122**, 1300–1320.
- Li Y., Dasgupta R. and Tsuno K. (2015) The effects of sulfur, silicon, water, and oxygen fugacity on carbon solubility and partitioning in Fe-rich alloy and silicate melt systems at 3 GPa and 1600 °C: implications for core-mantle differentiation and degassing of magma oceans and reduced planet. *Earth Planet. Sci. Lett.* **415**, 54–66.
- Li Y., Dasgupta R., Tsuno K., Monteleone B. and Shimizu N. (2016a) Carbon and sulfur budget of the silicate Earth explained by accretion of differentiated planetary embryos. *Nat. Geosci.* **9**, 781–785.
- Li Y., Marty B., Shcheka S., Zimmermann L. and Keppler H. (2016b) Nitrogen isotope fractionation during terrestrial coremantle separation. *Geochem. Perspect. Lett.*, 138–147.
- Libourel G., Marty B. and Humbert F. (2003) Nitrogen solubility in basaltic melt. Part I. Effect of oxygen fugacity. *Geochim. Cosmochim. Acta* 67, 4123–4135.
- Ma Z. (2001) Thermodynamic description for concentrated metallic solutions using interaction parameters. *Metall. Mater. Trans.* B 32, 87–103.
- Malavergne V., Bureau H., Raepsaet C., Gaillard F., Poncet M., Surblé S., Sifré D., Shcheka S., Fourdrin C., Deldicque D. and Khodja H. (2019) Experimental constraints on the fate of H and C during planetary core-mantle differentiation. Implications for the Earth. *Icarus* 321, 473–485.
- Mandeville C. W., Webster J. D., Rutherford M. J., Taylor B. E., Timbal A. and Faure K. (2002) Determination of molar absorptivities for infrared absorption bands of H2O in andesitic glasses. *Am. Mineral.* 87, 813–821.
- McCoy T. J. and Nittler L. R. (2014) Mercury. In *Treatise on Geochemistry*. Elsevier, pp. 119–126.
- Miyazaki A., Hiyagon H. and Sugiura N. (1995) Solubilities of nitrogen and argon in basalt melt under oxidizing conditions. AIP Conf. Proc. 341, 276–283.
- Morbidelli A., Lunine J. I., O'Brien D. P., Raymond S. N. and Walsh K. J. (2012) Building terrestrial planets. *Annu. Rev. Earth Planet Sci.* **40**, 251–275
- Mosenfelder J. L., Handt A., Der Vo, Füri E., Dalou C., Hervig R. L., Rossman G. R. and Hirschmann M. M. (2019) Nitrogen incorporation in silicates and metals: Results from SIMS, EPMA, FTIR, and laser-extraction mass spectrometry. Am. Mineral. 104, 31–46.
- Murphy P. J. and Roberts S. (1995) Laser Raman spectroscopy of differential partitioning in mixed-gas clathrates in H<sub>2</sub>O-C0<sub>2</sub>-N<sub>2</sub>-CH<sub>4</sub> fluid inclusions: implications for microthermometry. *Geochim. Cosmochim. Acta* **59**, 4809–4824.
- Mysen B. O. and Fogel M. L. (2010) Nitrogen and hydrogen isotope compositions and solubility in silicate melts in equilibrium with reduced (N+H)-bearing fluids at high pressure and temperature: Effects of melt structure. Am. Mineral. 95, 987– 999
- Mysen B. O., Fogel M. L., Morrill P. L. and Cody G. D. (2009) Solution behavior of reduced C-O-H volatiles in silicate melts at high pressure and temperature. *Geochim. Cosmochim. Acta* 73, 1696–1710.
- Mysen B. O., Kumamoto K., Cody G. D. and Fogel M. L. (2011) Solubility and solution mechanisms of C-O-H volatiles in silicate melt with variable redox conditions and melt compo-

- sition at upper mantle temperatures and pressures. *Geochim. Cosmochim. Acta* **75**, 6183–6199.
- Mysen B. O., Virgo D. and Seifert F. A. (1982) The structure of silicate melts: implications for chemical and physical properties of natural magma. *Rev. Geophys.* **20**, 353.
- Mysen B. O., Yamashita S. and Chertkova N. (2008) Solubility and solution mechanisms of NOH volatiles in silicate melts at high pressure and temperature – Amine groups and hydrogen fugacity. Am. Mineral. 93, 1760–1770.
- Odert P., Lammer H., Erkaev N. V., Nikolaou A., Lichtenegger H. I. M., Johnstone C. P., Kislyakova K. G., Leitzinger M. and Tosi N. (2018) Escape and fractionation of volatiles and noble gases from Mars-sized planetary embryos and growing protoplanets. *Icarus* 307, 327–346.
- Peplowski P. N., Klima R. L., Lawrence D. J., Ernst C. M., Denevi B. W., Frank E. A., Goldsten J. O., Murchie S. L., Nittler L. R. and Solomon S. C. (2016) Remote sensing evidence for an ancient carbon-bearing crust on Mercury. *Nat. Geosci.* 9, 273–276.
- Rai N. and Van Westrenen W. (2013) Core-mantle differentiation in Mars. J. Geophys. Res. E: Planets 118, 1195–1203.
- Rai N. and Van Westrenen W. (2014) Lunar core formation: new constraints from metal-silicate partitioning of siderophile elements. *Earth Planet. Sci. Lett.* 388, 343–352.
- Robert F. (2003) The D/H ratio in Chondrites. *Space Sci. Rev.* **106**, 87–101.
- Roskosz M., Bouhifd M. A., Jephcoat A. P., Marty B. and Mysen B. O. (2013) Nitrogen solubility in molten metal and silicate at high pressure and temperature. *Geochim. Cosmochim. Acta* 121, 15–28.
- Roskosz M., Mysen B. O. and Cody G. D. (2006) Dual speciation of nitrogen in silicate melts at high pressure and temperature: an experimental study. *Geochim. Cosmochim. Acta* 70, 2902–2918.
- Rubie D. C., Frost D. J., Mann U., Asahara Y., Nimmo F., Tsuno K., Kegler P., Holzheid A. and Palme H. (2011) Heterogeneous accretion, composition and core-mantle differentiation of the Earth. *Earth Planet. Sci. Lett.* 301, 31–42.
- Ruzicka A. and Hutson M. (2006) Differentiation and evolution of the IVA meteorite parent body: clues from pyroxene geochemistry in the Steinbach stony-iron meteorite. *Meteorit. Planet.* Sci. 41, 1959–1987.
- Sagan C. and Chyba C. (1997) The early faint sun paradox: organic shielding of ultraviolet-labile greenhouse gases. *Science* (80-.) **276**, 1217–1221.
- Sagan C. and Mullen G. (1972) Earth and Mars: evolution of atmospheres and surface temperatures. *Science* 177, 52–56.
- Schmidt B. C., Holtz F. M. and Bény J.-M. (1998) Incorporation of H2 in vitreous silica, qualitative and quantitative determination from Raman and infrared spectroscopy. *J. Non. Cryst. Solids* **240**, 91–103.
- Sen S., Widgeon S. J., Navrotsky A., Mera G., Tavakoli A., Ionescu E. and Riedel R. (2013) Carbon substitution for oxygen in silicates in planetary interiors. *Proc. Natl. Acad. Sci.* 110, 15904–15907.
- Silver L. A. (1988) Water in Silicate Glasses. Calif. Inst. Technol. Ph.D. Thes.
- Socrates G. (2001) Infrared and Raman Characteristic Group Frequencies-Tables and Charts.,
- Speelmanns I. M., Schmidt M. W. and Liebske C. (2019) The almost lithophile character of nitrogen during core formation. *Earth Planet. Sci. Lett.* 510, 186–197.
- Stanley B. D., Hirschmann M. M. and Withers A. C. (2011) CO<sub>2</sub> solubility in Martian basalts and Martian atmospheric evolution. *Geochim. Cosmochim. Acta* 75, 5987–6003.
- Stanley B. D., Hirschmann M. M. and Withers A. C. (2014) Solubility of COH volatiles in graphite-saturated martian basalts. *Geochim. Cosmochim. Acta* 129, 54–76.

- Steenstra E. S., Knibbe J. S., Rai N. and van Westrenen W. (2016) Constraints on core formation in Vesta from metal-silicate partitioning of siderophile elements. *Geochim. Cosmochim. Acta* 177, 48–61.
- Steenstra E. S., Sitabi A. B., Lin Y. H., Rai N., Knibbe J. S., Berndt J., Matveev S. and van Westrenen W. (2017) The effect of melt composition on metal-silicate partitioning of siderophile elements and constraints on core formation in the angrite parent body. *Geochim. Cosmochim. Acta* 212, 62–83.
- Stolper E. (1982) Water in silicate glasses: an infrared spectroscopic study. *Contrib. to Mineral. Petrol.* **81**, 1–17.
- Trail D., Watson E. B. and Tailby N. D. (2011) The oxidation state of Hadean magmas and implications for early Earth's atmosphere. *Nature* **480**, 79–82.
- Tsuno K., Grewal D. S. and Dasgupta R. (2018) Core-mantle fractionation of carbon in Earth and Mars: The effects of sulfur. *Geochim. Cosmochim. Acta* 238, 477–495.
- Wade J. and Wood B. J. (2005) Core formation and the oxidation state of the Earth. *Earth Planet. Sci. Lett.* **236**, 78–95.
- Wetzel D. T., Hauri E. H., Saal A. E. and Rutherford M. J. (2015) Carbon content and degassing history of the lunar volcanic glasses. *Nat. Geosci.* 8, 755–758.

- Wetzel D. T., Rutherford M. J., Jacobsen S. D., Hauri E. H. and Saal A. E. (2013) Degassing of reduced carbon from planetary basalts. Proc. Natl. Acad. Sci. 110, 8010–8013.
- Yang J. and Epstein S. (1983) Interstellar organic matter in meteorites. Geochim. Cosmochim. Acta 47, 2199–2216.
- Yoshioka T., McCammon C., Shcheka S. and Keppler H. (2015) The speciation of carbon monoxide in silicate melts and glasses. *Am. Mineral.* **100**, 1641–1644.
- Young E. D., Manning C. E., Schauble E. A., Shahar A., Macris C. A., Lazar C. and Jordan M. (2015) High-temperature equilibrium isotope fractionation of non-traditional stable isotopes: experiments, theory, and applications. *Chem. Geol.* 395, 176–195.
- Zhang C. and Duan Z. (2009) A model for C-O-H fluid in the Earth's mantle. *Geochim. Cosmochim. Acta* **73**, 2089–2102.
- Zolotov M. Y., Sprague A. L., Hauck S. A., Nittler L. R., Solomon S. C. and Weider S. Z. (2013) The redox state, FeO content, and origin of sulfur-rich magmas on Mercury. *J. Geophys. Res. E: Planets* 118, 138–146.

Associate editor: Christopher Herd